

1 High 1 km-resolution maps reveal increases in woody above- and
2 belowground forest biomass carbon pools in China from 2003 to
3 2020 over the past 20 years

4 Yongzhe Chen^{1,2}, Xiaoming Feng^{1,2,*}, Bojie Fu^{1,2}, Haozhi Ma³, Constantin M. Zohner³,
5 Thomas W. Crowther³, Yuanyuan Huang^{4,5}, Xutong Wu⁶, Fangli Wei¹

6 1 State Key Laboratory of Urban and Regional Ecology, Research Center for Eco-
7 Environmental Sciences, Chinese Academy of Sciences, Beijing, PR China.

8 2 College of Resources and Environment, University of Chinese Academy of Sciences, Beijing,
9 PR China.

10 3 Institute of Integrative Biology, ETH Zurich (Swiss Federal Institute of Technology), Zurich,
11 Switzerland.

12 4 Laboratoire des Sciences du Climat et de l'Environnement, LSCE/IPSL, CEA-CNRS-UVSQ,
13 Université Paris-Saclay, Gif-sur-Yvette, France

14 5 Commonwealth Scientific and Industrial Research Organisation, Aspendale, Victoria,
15 Australia

16 6 State Key Laboratory of Earth Surface Processes and Resource Ecology, Faculty of
17 Geographical Science, Beijing Normal University, Beijing, PR China.

样式定义: 正文

样式定义: EndNote Bibliography Title: 不检查拼写
或语法

样式定义: EndNote Bibliography: 不检查拼写或语法

18 *Correspondence authors: fengxm@rcees.ac.cnfengxm@rcees.ac.cn

19 **Abstract**

20 To quantify the ecological consequences of recent ~~nation-wide~~[nationwide](#) restoration efforts in
21 China, spatially-explicit information on ~~woody forest~~ biomass ~~carbon stock~~ changes over the
22 ~~21st century~~[past 20 years](#) is critical. However, long-term biomass tracking at the national scale
23 remains challenging as it requires continuous and high-resolution monitoring. Here, we
24 characterize the changes in ~~forests'~~ above- and belowground biomass (~~AGB~~[carbon \(AGBC](#) and
25 ~~BGB) for woody vegetation~~[BGBC](#)) in China between ~~2003~~[2002](#) and ~~2020~~[2021](#) at ~1 km spatial
26 resolution by integrating multiple types of remote sensing observations with intensive field ~~plot~~
27 measurements through ~~regression and~~ machine learning ~~and mixed-pixel decomposition~~
28 ~~methods/approaches~~. On average, ~~11.8.6 ± 0 ± 0.7.6~~ and ~~2.8 ± 0.2 ± 0.1~~ PgC ~~are~~[were](#) stored in
29 above- and belowground live ~~woody biomass~~[forests](#) in China. Over the last ~~1820~~ years, the total
30 ~~woody forest~~ biomass ~~carbon~~ ~~pool~~ in China has increased at a rate of ~~163.8~~[114.5 ± 16.3](#) TgC/yr
31 (~~0.5~~[approximately 1.1](#)%/yr). The most pronounced ~~forest~~ biomass ~~carbon stock~~ gains occurred
32 in central to southern China, including the southern Loess Plateau, Qinling Mountains,
33 southwest ~~karst~~[karsts](#) and southeast forests. ~~The~~[While the](#) combined use of ~~low-frequency~~
34 ~~microwaves and advanced laser~~[multi-source](#) remote sensing data provides a powerful tool to
35 assess ~~the forest~~ biomass ~~trends, minimizing under- or overestimation of biomass variation in~~
36 ~~space and time~~. ~~Future~~[carbon changes, future](#) research is ~~also~~ needed to explore the drivers of

37 the observed woody biomass trends, and to evaluate the degree to which biomass gains will
38 translate into biodiverse, healthy ecosystems and thus are sustainable.

39 **Key words:** Aboveground biomass [carbon pool](#); Belowground biomass [carbon](#); Long-term
40 continuous mapping; [Hotspot of amount and trend](#); China

41 **1 Introduction**

42 ~~Woody (forest and shrubland) biomass contributes to over 90% of global vegetation biomass~~
43 ~~(Ma et al. 2021). As a net outcome of carbon gains from photosynthesis and carbon losses from~~
44 ~~respiration, mortality and disturbances, woody biomass is a critical indicator of ecosystem~~
45 ~~function and services, such as carbon sequestration, wood production and resource allocation~~
46 ~~(Kumar and Mutanga 2017). Accurate biomass monitoring over space and time is thus essential~~
47 ~~for assessing ecosystem management strategies and mitigation policies (Kumar and Mutanga~~
48 ~~2017).—~~

49 ~~In recent decades, remote sensing tools have been integral in our efforts to map aboveground~~
50 ~~biomass (AGB). Forest biomass carbon stock contributes to over 90% of the global vegetation~~
51 ~~biomass carbon pool (Ma et al., 2021). As a net outcome of carbon gains from photosynthesis~~
52 ~~and carbon losses from respiration, mortality and disturbances, forest biomass carbon stock~~
53 ~~(approximately 50% of biomass) is a critical indicator of ecosystem function ~~hereinafter~~~~
54 ~~~~SVC~~mean and ecosystem services, such as carbon sequestration, wood production and~~
55 ~~resource allocation (Kumar and Mutanga, 2017). Accurate forest biomass carbon stock~~
56 ~~monitoring over space and time is thus essential for assessing ecosystem management strategies~~
57 ~~and mitigation policies (Kumar and Mutanga, 2017).—~~

58 ~~In recent decades, remote sensing tools have been integral in our efforts to map aboveground~~
59 ~~biomass (AGB) or carbon stock (AGBC). By combining satellite imagery (e.g., MODIS) and~~

60 airborne LiDAR signals, forest cover and canopy height can be mapped across large spatial
61 scales (Hu et al., 2016; Saatchi et al., 2011; Su et al., 2016; Tong et al., 2020; Xu et al., 2021).
62 Apart from ~~imageries~~optical images and LiDAR signals, microwaves can provide more detailed
63 insights into ~~sub-canopy~~subcanopy forest structure and AGBAGBC due to their ability to
64 penetrate the canopy. Active microwave techniques, i.e., Synthetic Aperture Radar (SAR)
65 backscatters, facilitate high-resolution (e.g., 100 m) AGB mapping, but the temporal coverage
66 is limited (Bouvet et al., 2018; Cartus et al., 2012; Bouvet et al., 2018). Conversely, vegetation
67 optical depth (VOD) retrieved from multiple passive microwave sensors can be used to produce
68 long-term continuous AGB maps (Frappart et al., 2020; Liu et al., 2011; Liu et al., 2015), yet
69 at a coarse spatial resolution (e.g., 0.25°). Because optical, LiDAR and microwave (both active
70 and passive)~~different~~ remote sensing techniques ~~all~~ have ~~different~~their advantages and pitfalls,
71 combining these techniques and complementing them with direct ground measurements is
72 integral to maximizing the accuracy and precision of biomass carbon estimations across space
73 and time.

74 Another source of uncertainty in vegetation biomass carbon stocks is the extent of biomass that
75 is stored belowground as roots. While AGBAGBC mapping is facilitated by ~~the~~a suite of
76 emerging remote sensing techniques, investigating the spatiotemporal variation in belowground
77 biomass (~~BGB~~carbon pool (BGBC) remains challenging despite the large contribution of ~~root~~
78 biomassroots to total carbon storage (Huang et al., 2021; Ma et al., 2021). To map BGBBGBC,
79 the commonly-used approach is to combine aboveground biomass information with vegetation

80 type-specific ratios of BGB to AGB (i.e., root-shoot ratio, or RSR) ([Xu et al., 2021](#); Saatchi et
81 al., 2011; [Xu et al. 2021](#)). ~~Because field studies indicate a near linear relationship between log-~~
82 ~~transformed BGB and AGB (Enquist Brian and Niklas Karl 2002), BGB variations at large~~
83 ~~scales have often been approximated using this relationship (Spawn et al. 2020). To capture the~~
84 ~~complex relationship between BGB and biotic or abiotic variables (e.g., stand age, heat and~~
85 ~~water availability), machine learning algorithms have been applied to map BGB (Huang et al.~~
86 ~~2021) and root mass fractions (Ma et al. 2021) globally. In mixed pixels with multiple plant~~
87 ~~functional types, BGB mapping relying on satellite-based AGB and plot-based models is~~
88 ~~expected to be less accurate. In addition, the existing woody plots are unevenly distributed~~
89 ~~across the world, with limited plots in developing countries, leading to large uncertainties in~~
90 ~~BGB estimation within those regions (Huang et al. 2021).~~

91 . Because field studies indicate a near-linear relationship between log-transformed BGB and
92 AGB (Enquist Brian and Niklas Karl, 2002), BGB variations at large scales have often been
93 approximated using this relationship (Spawn et al., 2020). To capture the complex relationship
94 between BGB and biotic or abiotic variables (e.g., stand age, heat and water availability),
95 machine learning algorithms have been applied to map BGB (Huang et al., 2021) and root-mass
96 fractions (Ma et al., 2021) globally. However, the reference plots were unevenly distributed
97 across the world, limited in developing countries, leading to some uncertainties in BGB and
98 BGBC estimation within those regions (Huang et al., 2021).

99 China has been implementing national-scale afforestation and reforestation programs since the
100 late 1990s (Lu et al., 2018)(Lu et al., 2018), promoting vegetation cover and carbon storage in
101 the Loess Plateau and the southwest karst regions, etc. (Chen et al., 2019a; Niu et al., 2019;
102 Tong et al., 2018). A spatial understanding of [woody forest](#) biomass trends can help evaluate
103 the efficiency of ecological restoration programs. High quality, high resolution and long-term
104 continuous woody biomass monitoring in China has remained challenging, ~~due to difficulties~~
105 ~~in integrating different remote sensing techniques with ground-sourced measurements~~ (Zhang
106 ~~et al., 2019; Huang et al., 2019; Zhang et al., 2019~~).

107 In this study, ~~we integrate different~~ [by integrating multi-source](#) remote sensing ~~tools (optical,~~
108 ~~active/passive microwave and LiDAR) data~~ with large quantities of plot measurements ~~through~~
109 ~~random forest approach to produce high-~~ [we produced 1 km](#) resolution (~~1 km~~)-above- and
110 belowground [woody forest](#) biomass [carbon pool](#) maps ~~in~~for China during ~~2003–2020, the past~~
111 ~~20 years (2002–2021)~~. This dataset could provide new insights into ~~the spatial hotspots of~~
112 ~~woody biomass and its interannual~~ [forest carbon stock](#) changes [in China](#) over the past two
113 decades.

114 **2 Materials and methods**

115 ~~To map above- and belowground woody biomass in China during 2003–2020, we 1) integrated~~
116 ~~state-of-the-art satellite derived forest AGB and canopy height information with ground-~~
117 ~~sourced plot data; 2) developed an improved vegetation water content (VWC) dataset covering~~

2003–2020 based on the intercalibration of vegetation optical depth retrieved from various microwave sensors; 3) combined multiple sources of remote sensing and in situ observations simultaneously allowing for both high resolution and long term mapping; 4) built a plot data-based random forest or regression model to estimate BGB based on AGB information; and 5) harmonized scale differences existing between plot measurements and satellite observations. The basic procedure is shown in Figure 1 and described in sections 2.1–2.5.

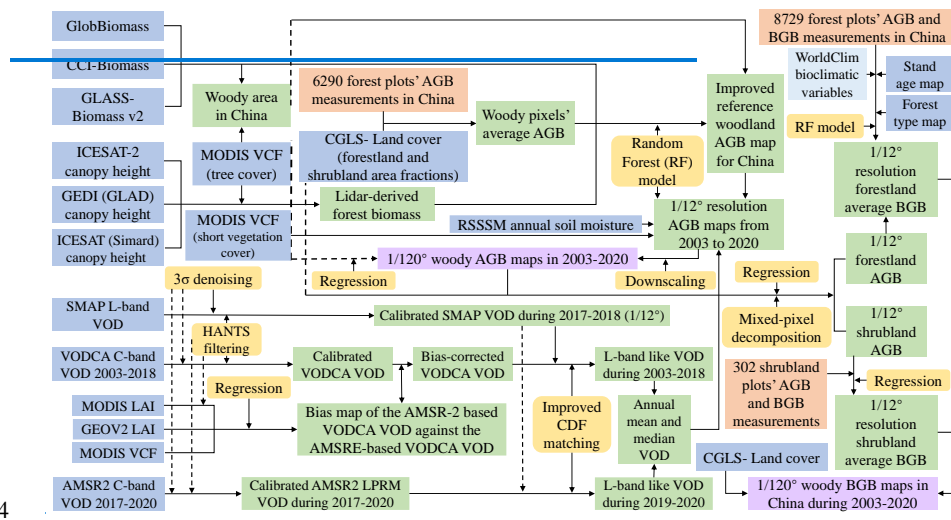


Figure 1. Workflow of woody AGB and BGB monitoring in China during 2003–2020. The blue rectangles are remote sensing based data inputs; orange rectangles are plot level measurements; yellow rectangles represent the key methods; while the purple rectangles represent the final output products of this study. ‘GlobBiomass’, ‘CCI’, etc. are data products’ names; ‘CDF’= ‘cumulative distribution function’; ‘HANTS’= ‘harmonic analysis of time series’; ‘VCF’= ‘vegetation continuous fields’. Locations of forest plots are shown in Figure S1a.

2.1 An improved benchmark map of aboveground biomass (AGB) in China

We used the three latest and highest quality global scale AGB datasets (GlobBiomass, CCI Biomass and GLASS Biomass v2) to derive our benchmark map. Using SAR, LiDAR and optical images, the first global high resolution (100 m) forest AGB dataset for the year 2018, GlobBiomass, was published through the European Space Agency (ESA)'s Data User Element (DUE) project (Santoro et al. 2021). The relative root mean square error (RMSE) was below 30%, although biomass tends to be underestimated in dense forests (Mialon et al. 2020). Subsequently, ESA's Climate Change Initiative (CCI) published a global AGB map for all vegetation in 2017 using a slightly different algorithm, followed by AGB maps for 2010, 2018 and 2019 (Santoro and Cartus 2019, 2021). Datasets derived from different methods have their advantages in different regions. By referring to adequate in situ data, we may combine the advantages of different datasets. Accordingly, integration of several high quality AGB maps has become popular. The Global Land Surface Satellite (GLASS) AGB v2 was developed by fusing the AGB maps in (Hu et al. 2016), (Su et al. 2016) and (Turner et al. 2014), etc., through the linear combination method. GLASS Biomass v2 roughly represents the AGB status in the year 2000, the median period of the collected woody plots' data (Zhang and Liang 2020).

We aggregated the GlobBiomass and CCI Biomass maps from $1/1125^\circ$ resolution to $1/120^\circ$ (approximately 1 km) and resampled the GLASS Biomass product from 0.01° to $1/120^\circ$. The study area, i.e., woody areas in China, was determined as all the $1/120^\circ$ pixels (note: the $1/120^\circ$

150 resolution is referred to as a pixel hereinafter) for which AGB data are available from each of
151 these three biomass datasets.

152 In September 2018, ICESat 2 provided an Advanced Topographic Laser Altimeter System
153 (ATLAS) that provides more accurate and denser measurements of canopy height than GLAS
154 (Markus et al. 2017). However, the application of ICESAT 2 data in canopy height estimation
155 at large scales is currently limited (Liu et al. 2022). This study selected the ATL08 land and
156 vegetation V004 product, and the 98% height retrievals of all canopy photons in each 100 m
157 segment can best represent the mean top canopy height (Neuenschwander et al. 2020). All
158 ATLAS records acquired in China's woody areas during 2018–2020 were incorporated. ATLAS
159 has three strong and three weak beams. According to previous studies, the canopy heights
160 retrieved using strong beams are generally more accurate than those retrieved by weak beams
161 (Neuenschwander et al. 2020). Hence, in each $1/120^\circ$ resolution pixel, we counted the numbers
162 of valid strong beam and weak beam observations within the pixel during 2018–2020. If the
163 number of strong beam records exceeded 5, then only those higher quality data were used.
164 Otherwise, if there were at least 5 valid observations, but the number of strong beam retrievals
165 was not enough, all data in the pixel were incorporated. Afterwards, we adopted the median
166 absolute deviation (MAD) method to detect and eliminate outliers (Leys et al. 2013). For the
167 remaining reliable canopy height retrievals in each pixel, we took the average weighted by the
168 corresponding canopy cover fractions. Here, the top canopy cover fraction was estimated as the
169 ratio of canopy photons to the number of all photons in the 100 m segment. By following the

170 above steps, we mapped forest height over China using ATLAS data. Because gaps remain
171 between the tracks of ICESAT 2, although ATLAS's six beams enable a larger spatial coverage
172 than any other LiDAR instrument, the derived forest height map provides values in only 42%
173 of all woody pixels in China. Because of the potentially bad LiDAR estimates, the highest 2.5%
174 extreme values were further excluded.—

175 Another new LiDAR instrument is NASA's Global Ecosystem Dynamics Investigation (GEDI).
176 It is optimized for global canopy height estimation, and has been collecting data in China since
177 April 2019 (Dubayah et al. 2020). However, the orbital gaps of GEDI are much larger than that
178 of ICESAT 2, resulting in limited spatial coverage by direct observation. Therefore, this study
179 adopted the Global Forest Canopy Height 2019 dataset provided by the Global Land Analysis
180 and Discover (GLAD). GLAD's canopy height was mapped by integrating the GEDI's forest
181 structure measurements globally with Landsat maps through machine learning (Potapov et al.
182 2020). The original 30 m resolution data were averaged to 1/120°. GEDI does not collect data
183 in north of 51.6°N (Dubayah et al. 2020), but the highest latitude of China is about 53.56°N.
184 Therefore, we used an alternative global gridded forest height map that was developed earlier
185 through machine learning, yet based on the ICESAT GLAS retrievals (Simard et al. 2011).—

186 Because AGB is more related to the forest volume rather than just the canopy height, we further
187 multiplied the three different LiDAR based canopy height maps with the percent of tree cover
188 (hereinafter TC) acquired from MOD44B v006 dataset. The products of multiplications are

189 hereinafter ATLAS-derived volume, GEDI-derived volume and GLAS-derived volume. None
190 of these LiDAR-based timber volumes cover all woodland pixels in China. Specifically, without
191 spatial interpolation using optical remote sensing, the ATLAS-derived volume inherited the
192 orbital gaps of ICESAT 2, although the quality is expected higher than that of the other two
193 machine learning-derived canopy heights and volumes. Thus, we designed three random forests
194 for AGB estimation. Each of these three random forests (RFs) have four input predictors.
195 GlobBiomass, CCI-Biomass and GLASS-Biomass v2, are incorporated as the predictors of
196 each RF, while the use of which LiDAR-derived volume as the 4th input predictor makes the
197 difference among the three RFs. Moreover, to reduce uncertainties in LiDAR-derived timber
198 volumes, the pixels with tree cover below 5% are classified as nonwoody areas and excluded.

199 The training target should be a large number of high-quality 1/120° pixel-scale AGB data in
200 China. This study collated forest or shrubland plots' AGB calculated using allometric equations
201 or clear-cutting methods from various published papers, including (Luo 1996), (Luo et al. 2014),
202 (Guo and Ren 2014), (Peng et al. 2016), (Wang et al. 2014), (Guo et al. 2021), (Yang et al.
203 2017), (Liu et al. 2020) and (Nie et al. 2016). In addition to AGB, we recorded the BGB, stand
204 age, vegetation species or type and location information. The spatial distributions of all these
205 woody plots are shown in Figure S1a. Some records were measured in 1990–2000, whereas
206 others were acquired during 2000–2010. Because plots smaller than 0.05 ha are not comparable
207 to satellite observations (Su et al. 2016), 10 m×10 m plots (Guo and Ren 2014) were not
208 included as the training target here, but were applicable in determining the biomass allocation

209 rule later in section 2.5. Moreover, the understory shrub AGB was excluded, since SAR and
210 LiDAR can observe only the canopy. The extreme values (the highest and lowest 1%) were
211 excluded as well. These filters resulted in 6290 woody plots remaining. Because the plots are
212 mainly located in woodlands, yet the corresponding pixel usually contains cropland, urban,
213 waters or bare ground, whose AGB are much lower than those in the plots, we converted the
214 plot level AGB into the pixel scale AGB by multiplying the area fraction of forestland in the
215 pixel, as long as the forestland area fraction exceeds 20% and is larger than the shrubland area
216 fraction. Here, land cover type comes from the Copernicus Global Land Service: Land Cover
217 100m (CGLS LC) epoch 2017: v3.0.1 product (Buehner et al. 2020). It includes not only
218 discrete land cover classification but also the fractions of forestland, shrubland, grassland and
219 cropland at 100 m resolution. We aggregated these high resolution land cover fractions to $1/120^\circ$
220 to reduce the uncertainties. It should be noted that VCF data cannot be applied here because
221 they indicate the fractions of pure tree cover and short vegetation cover, yet a forestland contains
222 bare ground or herbs among trees.

223 The RF model trainings were conducted in MATLAB R2021a software. After the RF trainings,
224 three sets of simulations were performed using the corresponding RF model in woody pixels
225 where all four predictors (three existing AGB products and one LiDAR derived volume) have
226 valid data. In addition, we performed ten fold cross validation to assess the performance of
227 each RF model, and took the averages of ten times of simulations. Finally, we combined the
228 three sets of simulations by averaging that is weighted by the mean R^2 of the corresponding RF

229 model. Using above methods, we produced a spatially continuous 1/120° benchmark AGB map
230 for China. Because most of these measurements refer to the vegetation biomass status in around
231 2000, we expect our AGB map to represent the AGB in around 2000. Therefore, our improved
232 benchmark AGB map is hereinafter named ‘AGBbenchmark_2000s’.

233 In addition, we exported the importance of each predictor variable in the RF models. For any
234 variable, the measure is the increase in prediction error if the values of that variable are
235 permuted across the out-of-bag observations. This measure is computed for every tree, then
236 averaged over the entire ensemble and divided by the standard deviation of the entire ensemble.

237 **2.2 An improved vegetation optical depth dataset covering 2003–2020**

238 To derive a long time series of AGB, long term continuous microwave VOD (i.e., vegetation
239 opacity) data is useful (Jackson and Schmugge 1991; O'Neill et al. 2021). Through cumulative
240 distribution function (CDF) matching among different VOD products, the vegetation optical
241 depth climate archive (VODCA) was developed (Moesinger et al. 2020). The ‘C band’ product
242 which was retrieved using several C band microwave sensors including AMSR-E, WindSat and
243 AMSR2 and covers 2003–2018, is a better indicator of the whole woody plants’ biomass than
244 those retrieved using higher frequency microwave bands (i.e., X band and Ku band). However,
245 compared to the VOD retrieved from L band sensors such as SMOS (Wigneron et al. 2021) and
246 SMAP (Konings et al. 2017), C band VODs are still less sensitive to the biomass of trunks and
247 branches, which contribute most to the AGB (Li et al. 2021). Therefore, C band VODs usually

248 have high frequency variations due to the strong variation in leaf water content per biomass
249 under rainfall or drought events (Li et al. 2021). In addition, VODCA's C-band product is not
250 perfectly continuous. Because the AMSR2 sensor does not share any temporal overlap with
251 AMSR-E, the rescaling of AMSR2 data towards AMSR-E was based on the assumption that
252 VOD remained stable over 2010–2013, i.e., the last and first two years of both sensors. For
253 China where land use cover changes were prevalent, this assumption may lead to a bias of
254 AMSR2-based VODCA data during 2013–2018 compared to the values in this period if the
255 retrievals from AMSR-E were available. Theoretically, this bias is spatially variable, and is
256 positively correlated with local VOD changes from 2010 to 2013. Thus, to develop an improved
257 VOD dataset covering 2003–2020 for China, we focused on 1) filtering out the high frequency
258 fluctuations in VODCA's product and other C-band VOD products; 2) mapping and correcting
259 the bias of AMSR2-based VODCA data during 2013–2018 compared to the AMSR-E based
260 VODCA VOD; 3) rescaling the C-band VODs against L-band VOD data to make their spatial
261 patterns more correlated with that of woody plants' AGB; 4) extending the VODCA dataset to
262 2020 by using AMSR2 observations. Details are as follows.

263 Due to a very high level of radio frequency interference (RFI), SMOS data are noisy and even
264 missing in China, especially in eastern China (Wigneron et al. 2021), making it inapplicable to
265 this study despite its longer time series than SMAP. SMAP observations have been available
266 since April 2015, so this study utilized the data from 2016 to 2020. The dual channel algorithm
267 (DCA) derived VOD data included in the SMAP Enhanced L3 v5 product (O'Neill et al. 2021)

268 were resampled from 9 km resolution to 1/12°. For each 1/12° grid cell (note: 1/12° resolution
269 is hereinafter called a grid cell) where at least 609 (i.e., 1/3 of 1827 daily maps in 5 years) valid
270 VOD retrievals are available, we first filtered the abnormal values using ‘3 σ denoising’ (Chen
271 et al. 2021). Second, we virtually filled in the data in 2015 and 2021 by using those in 2016 and
272 2020. Subsequently, the no data values resulting from orbital gaps or frozen states were filled
273 by linear interpolation, while the outputs during 2016–2020 were supposedly valid. Moreover,
274 we also determined the average annual number of VOD peaks for each grid after setting the
275 thresholds of minimum distance between two peaks, peak height and dominance of peaks to
276 reasonable values. Specifically, for grid cells where woody plants exist yet without VOD data,
277 the values were filled by sequentially searching and averaging nearby valid values (Chen et al.
278 2019b). For VODCA’s C-band VOD during 2003–2018, after filtering out the abnormal values
279 and virtually filling the data in 2002 and 2019, we performed the Harmonic Analysis of Time
280 Series (HANTS) filtering (Menenti et al. 1993; Roerink et al. 2000). Either high or low outliers
281 were excluded, while the number of frequencies to be considered above zero frequency in the
282 Fourier function was set to the product of the mean annual peak number detected by SMAP
283 VOD and the number of years.

284 We then mapped the bias of AMSR2-based VODCA’s VOD compared to the AMSR-E based
285 VODCA VOD data in 2003–2011. Because annual VOD is closely related to the leaf area index
286 (LAI), and is clearly affected by percent tree cover and percent nontree vegetation (i.e., crops,
287 grass and shrubs) cover, we performed a multiple linear regression between annual medians of

288 adjusted VODCA VOD data during the period of 2003–2011 and annual LAI values as well as
289 VCF retrievals. This study employed LAI from two sources. First, we processed the potential
290 cloud-affected values within the MODIS LAI product (MCD15A2H v006) by masking the
291 values flagged by clouds and then performing HANTS filtering, with low outliers excluded and
292 the number of frequencies set to 3 times the number of years. Second, for the LAI developed
293 by the ESA Copernicus Global Land Service (GEOV2 LAI) (Baret et al. 2013; Verger et al.
294 2014), we harmonized the retrievals from the SPOT-VGT sensor during 2003–2013 and those
295 from the PROBA-V sensor after 2014 using CDF matching with MODIS data applied as the
296 reference (Cammalleri et al. 2019). The MODIS LAI, VCF and GEOV2 LAI were all averaged
297 from their original spatial resolutions (250m–1km) to 0.25° to match the resolution of VODCA.
298 As shown in Figure S2a–b, after the regression, the R^2 values of 90% grids exceeded 0.3, and
299 the grid-specific regression coefficients were exported. Therefore, the mean bias of AMSR2-
300 based VODCA data during 2013–2018 compared to that before 2012 could be estimated as the
301 difference between the mean annual VOD calculated based on the above regression coefficients
302 as well as LAI and VCF data during 2013–2018 and the mean value of the adjusted VODCA's
303 medians over that period. This bias was positive in most areas of China, especially afforested
304 areas, such as northern Beijing (Figure S2c–d). Accordingly, by adding this bias to the VODCA
305 VOD data after 2013, we improved its temporal continuity.

306 Using SMAP's 1/12° VOD data during 2017–2018 as the reference, we calibrated the spatial
307 pattern of the adjusted VODCA VOD by rescaling. Notably, we revised the CDF matching

308 algorithm (Moesinger et al. 2020). For either the lowest or the highest 10% of the time series,
309 a linear fitting model was designed and applied, to eliminate abnormally low or high values.
310 Finally, to ensure a temporally consistent VOD time series from 2003 to 2020, for 2019 and
311 2020, we adopted the AMSR2 C band VOD and converted it into L band like VOD by referring
312 to SMAP data. Here, we chose the AMSR2/GCOM-W1 surface soil moisture (LPRM) L3 1 day
313 10 km x 10 km descending V001 dataset, and resampled it to 1/12° resolution. Upon noticing
314 sharp changes in AMSR2 VOD at the beginning of 2016 in many grid cells in China, this study
315 selected the records from only 2017–2020, which were calibrated and resealed later through
316 improved CDF matching by referring to the SMAP's VOD during 2017–2018.

317 Using the temporally continuous and spatially L band like VOD dataset from 2003 to 2020, we
318 calculated both annual mean and median VOD values as two robust indicators of annual AGB.

319 **2.3 High-resolution woodland AGB mapping in China from 2003 to 2020**

320 We performed two steps to map woodland AGB in China during 2003–2020. For the first step,
321 AGBbenchmark 2000s and VCF data in 2003 were all resampled to 1/12° resolution, the same
322 as VOD data. Specifically, for grid cells in which less than 50% of pixels were without valid
323 AGBbenchmark 2000s values due to limited forest cover, resampling was not performed.
324 Because VOD is influenced by the soil water availability, we built a random forest in which the
325 predictors include: mean and median VOD values, VCF data (i.e., TC and all vegetation cover,
326 hereinafter denoted as VC) and the mean surface soil moisture (SSM) in 2003. Here, SSM was

327 derived from a long-term remote sensing-based surface soil moisture (RSSSM) developed in
328 our previous study (Chen et al. 2021). The training target is the resampled AGBbenchmark
329 2000s. More than 80000 grids all across China were available for the training of this RF model.
330 Afterwards, using VOD, VCF and SSM in each year, we performed 1/12° resolution AGB
331 simulations over 2003–2020 along with ten-fold cross-validations, and adopted the mean of ten
332 independent simulations. We also calculated the ‘calibration factor’ which is defined as the ratio
333 of resampled AGBbenchmark 2000 (i.e., the training target) to the simulated AGB in 2003 in
334 every grid. Then, we multiplied the annual 1/12° resolution AGB in China during 2003–2020
335 with the grid-specific ‘calibration factor’.

336 For the next step, we downscaled the 1/12° resolution AGB to 1/120°. Here, it is assumed that
337 within a grid cell, the heights of trees are similar, while the short vegetation’s heights are also
338 similar. So, within a 1/12° grid cell, the AGB per tree cover (TC) and AGB per short vegetation
339 cover (SC) can both be considered constants. Hence, we performed a binary linear regression
340 between the AGBbenchmark 2000s value in each 1/120° pixel within the grid cell and the
341 corresponding VCF (TC and SC) values. The intercept (i.e., constant term) was excluded, so
342 the derived two regression coefficients can represent the mean values of AGB per TC and per
343 SC in the grid cell. For more than 75% of all grid cells, the regression R^2 exceed 0.5. Since
344 VCF indicates the coverage of pure tree and non-tree vegetation, AGB per TC should be higher
345 than that per SC. Therefore, for grid cells where the derived AGB per TC was smaller than the
346 AGB per SC, grids where either one of the regression coefficients was negative, or those

347 without very significant regressions (i.e., $p > 0.01$ or $R^2 < 0.1$), the regression was considered
348 invalid. The AGB per TC and AGB per SC in those grid cells were filled later by searching for
349 nearby valid regression results, while the R^2 values of those valid regressions were applied as
350 the weights in averaging the nearby valid values. The maps of AGB per TC and per SC in 2003
351 are shown in Figure S3. By integrating these data with pixel-scale VCF, we calculated the AGB
352 of all woody vegetation in each $1/120^\circ$ pixel, which was averaged to the AGB at $1/12^\circ$
353 resolution. Accordingly, the ratio of the grid-scale AGB calculated in the first step to the
354 aggregated AGB derived in this step can be used to further calibrate the high-resolution AGB
355 data. Finally, by repeating the procedures, we mapped woody AGB in China at $1/120^\circ$
356 resolution from 2003 to 2020.

357 **2.4 Mixed-pixel AGB decomposition towards scale matching**

358 We mapped AGB in China at $1/120^\circ$ pixel resolution, which is quite larger than the scale of plot
359 measurements. The collected plot level data usually represent the AGB and BGB per area in a
360 forest or shrubland with basically uniform landscapes (i.e., the density of trees/shrubs is even
361 in the plot, which can be either low or high). However, within a pixel, forests, shrubs, crops,
362 herbs and bare ground may coexist. It is known that the relationship between BGB and AGB in
363 forests differs from that in shrublands. Generally, shrub species have a much higher RSR than
364 trees (Qi et al. 2019; Tang et al. 2018). Hence, we tried to solve that ‘mixed pixel problem’ by
365 decomposing the simulated AGB in woody regions into the AGB per forestland area and the

366 AGB per shrubland area. Then, we applied the respective relationships between BGB and AGB
367 to transform the decomposed per-area AGBs into per-area BGBs for different types of forests
368 and shrublands. Afterwards, we multiplied the per-area BGBs with the corresponding area and
369 summed the products (i.e., all forestlands' BGB and shrublands' BGB). By this method, we
370 basically achieved scale matching between remote sensing and plot-level observations.

371 AGB decomposition generally followed the idea we proposed in a previous article (Chen et al.
372 2019b). Specifically, in woody grids, we counted the numbers of pixels with forests (i.e., pixels
373 in which the forestland area percentage was >10% according to the CGLS-LC) and those with
374 shrublands (shrubland area percentage >10%). For grid cells where there were at least 50 pixels
375 with forestland and 50 pixels with shrubland, we performed a binary linear regression without
376 intercept between all these pixel-scale AGB data and the area percentages of forestland and
377 shrubland in every woody pixel. Afterwards, the average per-area BGB for forestland and
378 shrubland in woody grid cells can be estimated as the corresponding regression coefficients.
379 However, the regression was supposed invalid when either regression coefficient was negative,
380 or the significance p-value exceeded 0.05, or R^2 was below 0 (R^2 can be negative for regressions
381 without constants due to the potential significant bias in AGB data). For these grids, a constant
382 term was further added to the regression if a valid result could be derived under this situation.
383 Specifically, for 1/12° grids with less than 50 pixels with forests, but the pixels with shrubland
384 are sufficient, we can reliably estimate the AGB per area shrubland as the ratio of grid-average
385 AGB to the mean shrubland area percentage in the grid. Similarly, the forestland per area AGB

386 in grids with only enough pixels with forests can be estimated by simply neglecting the few
387 shrubs. According to Figure S4a–b, complete AGB decomposition was achieved in 36% of all
388 grids with enough woody pixels, and the grid cells with reliable AGB estimates accounted for
389 61%. The invalid decompositions composed only 3%, which were filled later by sequentially
390 searching and averaging nearby valid results (88% of the valid regressions are with R^2 higher
391 than 0.5, see Figure S4c–d). Subsequently, we deleted both the highest and lowest 2.5% values
392 of all gridded per-area AGB estimates in China, and then filled those values. Finally, a mean
393 filter with a window size of 3×3 was applied for spatial smoothing. The final maps of AGB per
394 area forestland and that per shrubland area in around 2017 (note: CGLS LC data represent the
395 land cover around 2017) are shown in Figure S5. Within a grid cell, the per-area forestland's
396 AGB is usually (71% in China) higher than the corresponding per-area shrubland AGB, except
397 in mountains around the Sichuan Basin and some karst regions in southwestern China where
398 shrubs are probably much denser than trees. Because the average forestland area percentage in
399 woody grids in China (55%) is greater than the CGLS LC's mean shrubland area percentage
400 (13%), the average forestlands' AGB calculated based on the decomposition result (63.4 t/ha)
401 is much larger than the mean shrublands' AGB (11.6 t/ha in around 2017), which is reasonable.
402 After the decomposition, some per-area AGBs were filled in values, while some were derived
403 from linear regressions with intercepts. Therefore, the sum of forestland AGB and shrubland
404 AGB in approximately 2017 may not be equal to the total grid AGB at the same time before
405 decomposition. In addition, the sum of the decomposed AGBs in 2017 was obviously different

406 from the pre-decomposed AGB in other years. To solve this problem, we defined and calculated
407 another ‘calibration factor’ as the ratio of the simulated grid-scale AGB in any year from 2003
408 to 2020 before mixed-pixel decomposition to the grid’s AGB in 2017 after the decomposition.
409 Accordingly, by referring to the per-area forestland/shrubland AGB in 2017 and this ‘calibration
410 factor’ in each separate year, we could decompose the annual simulated-pixel-scale AGB into
411 the 1/120° resolution AGBs of forests and shrublands and the per-area forestland/shrubland’s
412 AGB over the whole study period.

413 **2.5 BGB mapping in China during 2003–2020 based on its relationship with AGB**

414 In this study, we collected 8729 and 302 records of both AGB and BGB in forest and shrubland
415 plots, respectively, throughout China (section 2.1). For forest plots, the BGB–AGB relationship
416 follows: $\log(\text{BGB})=0.93\times\log(\text{AGB})-0.51$, while the relationship for shrubland plots follows:
417 $\log(\text{BGB})=0.96\times\log(\text{AGB})-0.20$, and the regression R^2 are 0.92 and 0.85, respectively (Figure
418 S6). The number of forest plots is large enough, and the forest type and stand-age information
419 are both available at 8182 plots (~94% of all forest plots). Therefore, we trained an RF model
420 for estimating per-area forestland’s BGB annually.

421 In the RF model, the training target is the per-area BGB at 8182 forest plots, while the predictors
422 included not only forest plots’ per-area AGB, forest type (hereinafter FOR_T), stand age, but
423 also mean annual temperature (MAT), temperature seasonality (standard deviation of monthly
424 temperature $\times 100$, abbreviated as Tsea), mean annual precipitation (MAP) and precipitation

425 seasonality (coefficient of variation of monthly precipitation, P_{sea}). These climatic factors can
426 be obtained from the corresponding papers, or estimated from the WorldClim v2.1 dataset (Fick
427 and Hijmans 2017). In this study, FOR_T includes evergreen broadleaf forest (EBF), deciduous
428 broadleaf forest (DBF), evergreen needleleaf forest (ENF), deciduous needleleaf forest (DNF),
429 and mixed forest (MF), and was determined based on the major tree species in the plot. After
430 the RF training, to simulate grid-scale per-area forestland's BGB annually, apart from importing
431 WorldClim v2.1's MAT, T_{sea} , MAP, P_{sea} and the decomposed per-area forestland AGB in each
432 year into the RF model, we also inputted the forest stand age map for China (Zhang et al. 2017)
433 and the annual forest type map during 2003–2020, which was determined from the ESA CCI's
434 global 300-m-resolution annual land cover classification v2.0.7cds-v2.1.1 (Li et al. 2018).

435 Because shrubland plots are relatively limited, and the species and stand age information was
436 hardly provided, we directly converted the decomposed shrublands' per-area AGB into the per-
437 area BGB during 2003–2020 using the above regression relationship. Finally, by referring to
438 the forestland and shrubland area percentages in the CGLS-LC dataset, we mapped the annual
439 woody BGB in China at 1/120° resolution.

440 In addition, we also calculated the relative errors and uncertainties of AGB and BGB in each
441 year during 2003–2020 (see section 3.4).

442 **2.6 Data comparison and verifications**

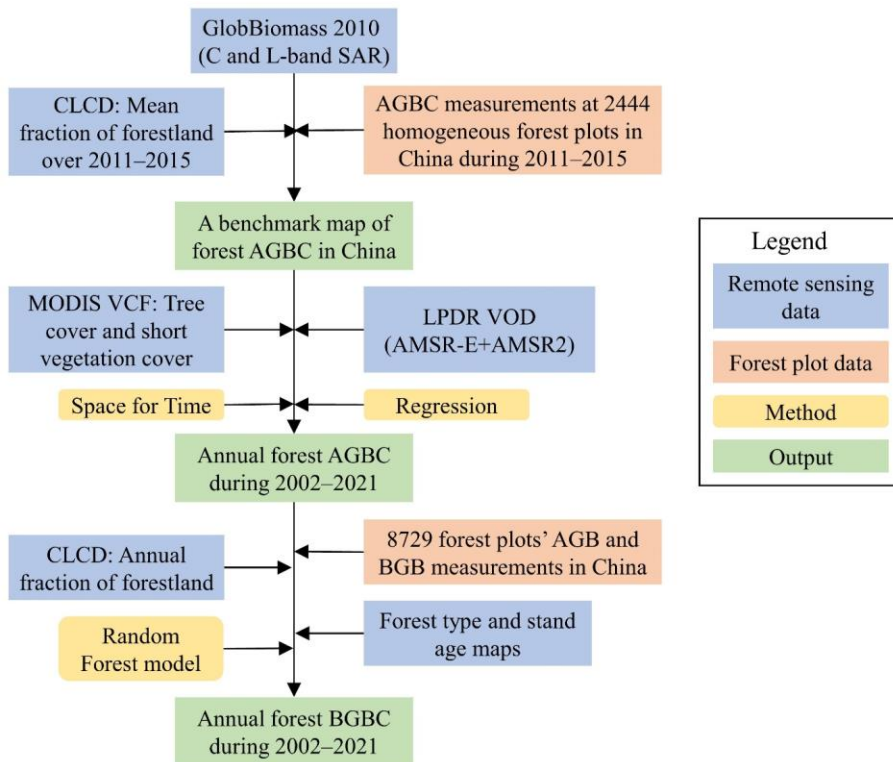
443 Apart from cross-validations based on woody plots' AGB and BGB measurements over China,

444 we further verified our AGB and BGB estimates by referring to the results of Tang et al., who
445 established 7800 forest plots and 1200 shrubland plots throughout China and then utilized the
446 random forest approach to spatially map AGB and BGB (Tang et al. 2018). Various statistics
447 were reported, e.g., the AGB, BGB and RSR for each woody vegetation type. Therefore, using
448 the discrete land cover classification map in the CGLS-LC dataset, we classified China's woody
449 ecosystems into six woody ecosystem types, i.e., EBF, DBF, ENF, DNF, MF and shrubland
450 (SHR) ecosystems, according to the majority in every pixel (Figure S7). The EBF, DBF, ENF,
451 DNF, MF and SHR ecosystems account for 59.6%, 18.4%, 15.3%, 6.1%, 0.1% and 0.5%,
452 respectively, of the total woody area in China. Because the MF and SHR ecosystems both have
453 very limited areas, this study just compares the AGB and BGB per area among the four major
454 forest ecosystems in China. Similarly, the change in woody biomass or carbon stock in China
455 can be verified by several measurements and remote sensing based studies (Fang et al. 2018;
456 Qiu et al. 2020; Xu et al. 2018).

457 We also compared the calculated spatial pattern of woody biomass and its trend against that of
458 existing global/regional long-term woody biomass datasets, including the well-received global
459 long-term AGB between 1993–2012 (Liu et al. 2015) and an updated woody biomass dataset
460 covering 2001–2019 (Xu et al. 2021).

461 Finally, to map above- and belowground forest biomass carbon stock in China during 2002–
462 2021, we 1) calibrated a SAR-based high-resolution forest aboveground biomass map in China

463 [based on massive field measurements of AGBC during 2011–2015; 2\) extended the AGBC time](#)
 464 [series to 2002–2021 by referring to the tree and short vegetation cover retrieved from optical](#)
 465 [remote sensing; 3\) calibrated the AGBC time series in some specific areas using a long-term](#)
 466 [integrated microwave-based VOD dataset; and 4\) mapped forestlands' BGBC through a random](#)
 467 [forest model developed based on the in-situ records in published literature. The basic procedure](#)
 468 [is shown in Figure 1 and described below.](#)



469 **Figure 1.** Workflow of forest biomass carbon pool monitoring in China during 2002–2021.
 470 [AGBC, BGBC: aboveground and belowground biomass carbon; VCF: vegetation continuous](#)
 471 [AGBC, BGBC: aboveground and belowground biomass carbon; VCF: vegetation continuous](#)

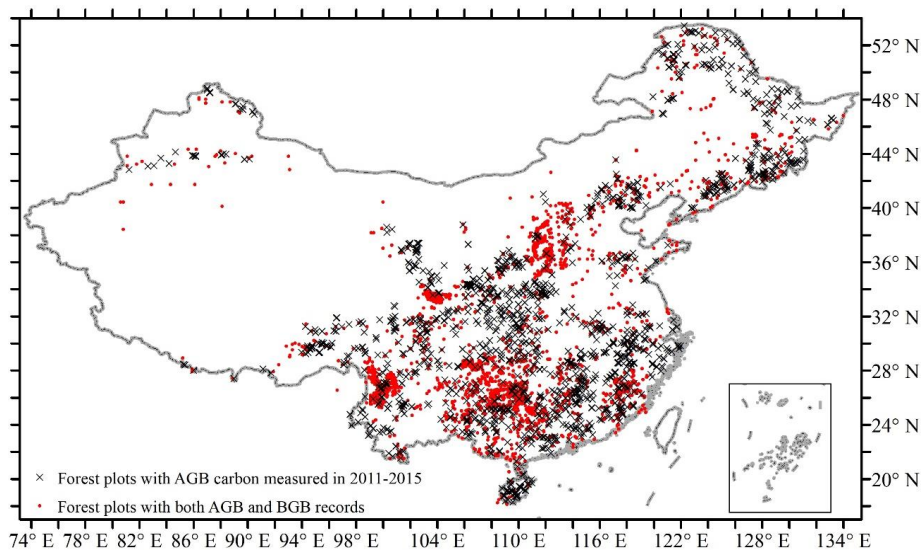
472 [fields; LPDR VOD: global land parameter data record- vegetation optical depth; CLCD: China](#)
473 [Land Cover Dataset](#)

474 **[2.1 A benchmark map of forest aboveground biomass carbon \(AGBC\) in China](#)**

475 [By combining multiple satellite observations of SAR backscatter, including the L-band ALOS](#)
476 [PALSAR and C-band Envisat ASAR around the year 2010, the first global high-resolution \(100](#)
477 [m\) forest AGB dataset, GlobBiomass 2010, was published through the European Space Agency](#)
478 [\(ESA\)'s Data User Element project \(Santoro et al., 2021\), whose relative root mean square error](#)
479 [\(RMSE\) was below 30% \(Mialon et al., 2020\). Apart from GlobBiomass 2010, another high-](#)
480 [resolution \(30 m\) forest AGB for China was produced by relating the ICESat GLAS \(LiDAR\)-](#)
481 [derived footprint AGB to various variables derived from Landsat optical images \(Huang et al.,](#)
482 [2019\). Because the ICESat data in 2006 were applied as the training target of the random forest](#)
483 [model, Huang's dataset refers to the AGB status in 2006. According to a recent validation study,](#)
484 [GlobBiomass and Huang's AGB performed the best among all existing AGB datasets in China](#)
485 [\(Chang et al., 2021\). Mean forest canopy heights and tree coverage are also good indicators of](#)
486 [the spatial pattern of forest biomass. The high-resolution \(30 m\) forest canopy height map for](#)
487 [China was developed by interpolating the ICESat-2 and GEDI data in 2019 through a neural](#)
488 [network \(Liu et al., 2022\), while the tree cover map at the same resolution was derived from](#)
489 [cloud-free growing season composite Landsat 7 data in around 2010 \(Hansen et al., 2013\). We](#)
490 [resampled GlobBiomass from 100 m resolution \(1/1125°\) to 1/1200° \(approximately 90 m\),](#)
491 [and averaged Huang's AGB map, canopy height map and tree cover map to the same resolution.](#)

492 [A reviewable, consistent ecosystem carbon stock inventory was conducted in China between](#)
493 [2011 and 2015 \(Tang et al., 2018\). We requested the AGB carbon stock \(AGBC\) data at more](#)
494 [than 5,000 30×30 m sized forest plots from the authors. Due to the scale mismatch between the](#)
495 [maps of biomass, canopy height or tree cover and the field measurements, we dropped out the](#)
496 [data within the 1/1200° resolution grids in which the standard deviation of tree cover was](#)
497 [greater than 15%, according to \(Chang et al., 2021\), leaving 2444 homogeneous forest plots](#)
498 [remaining \(see Figure 2 for the spatial distribution of these forest plots and Figure S1a~b for](#)
499 [the cumulative frequency curve and histogram of the AGBC records\). The AGBC records in](#)
500 [these forest plots were further multiplied by the mean fraction of forestland over 2011–2015 in](#)
501 [the corresponding grid, which was computed from the annual 30 m resolution China Land](#)
502 [Cover Dataset \(CLCD\) \(Yang and Huang, 2021\). By comparison, GlobBiomass 2010 AGB](#)
503 [matches the best with the grid-scale forest AGBC derived from plot measurements, with a](#)
504 [correlation coefficient \(CC\) of 0.50, followed by tree cover \(CC=0.42\), the product of canopy](#)
505 [height and tree cover \(CC=0.38\), and finally the canopy height \(0.27\) and Huang’s AGB \(0.25\).](#)
506 [Therefore, to obtain an improved benchmark map of forest AGBC in China for the period of](#)
507 [2011–2015, we chose the GlobBiomass 2010 dataset as our basis, and calibrated it against the](#)
508 [in-situ observation-based grid-scale forest AGBC. To build an equation for the calibration, we](#)
509 [divided the grid-scale AGBC values into 16 equidistant subranges \(0~15, 15~30, ..., 225~240](#)
510 [tC/ha\), calculated the median of grid-scale AGBC values that are within each subrange, and](#)
511 [then the median of GlobBiomass AGB values in the corresponding grids. According to previous](#)

512 [studies, an exponential function would be suitable for calibrating the GlobBiomass map in a](#)
513 [region such as China \(Mialon et al., 2020\). After the calibration, we averaged the benchmark](#)
514 [AGBC map from 1/1200° to 1/120° \(approximately 1 km\) to further reduce the uncertainties.](#)



516 [Figure 2. The spatial distribution of 1\) 2444 homogeneous forest plots with aboveground](#)
517 [biomass carbon stock measured between 2011 and 2015; and 2\) 8182 forest plots with](#)
518 [both above- and belowground biomass records collated in this study.](#)

519 [2.2 Temporally continuous forest AGBC mapping during 2002–2021](#)

520 [Because the benchmark AGBC was mapped based on SAR data, the spatial pattern accuracy is](#)
521 [guaranteed, but the temporal coverage is limited to just a few years. Hence, to create a forest](#)
522 [AGBC time series over the past 20 years, we integrated the benchmark AGBC with long-term](#)

523 [continuous optical and passive microwave remote sensing data.](#)

524 [The spatial resolution of optical remote sensing is higher, and is thus preferred in this study. By](#)
525 [adopting the MODIS vegetation continuous fields \(VCF\) data \(MOD44B v061\) which includes](#)
526 [three ground cover components: percent tree cover, percent non-tree vegetation \(i.e., short](#)
527 [vegetation\) cover, and percent non-vegetated \(Dimiceli et al., 2022\), we first calculated the](#)
528 [mean tree cover \(hereinafter, \$TC_{mean}\$ \) and short vegetation cover \(hereinafter \$SVC_{mean}\$ \) during](#)
529 [2011–2015, and resampled them from 250 m to \$1/120^\circ\$, the same resolution as the benchmark](#)
530 [AGBC map for 2011–2015. Because the canopy heights of trees are usually similar within a](#)
531 [small area, the regional AGBC per \$TC_{mean}\$ can be assumed as the same, which is referred to as](#)
532 [the ‘homogeneous assumption’ hereinafter. Accordingly, for each grid, we searched the \$TC_{mean}\$,](#)
533 [\$SVC_{mean}\$ and AGBC within a \$3\times 3\$ window \(\$1/40^\circ\times 1/40^\circ\$ \), and then regressed the AGBC values](#)
534 [in 9 grids against both \$TC_{mean}\$ \(the primary, or key predictor of AGBC\) and \$SVC_{mean}\$ \(assumed](#)
535 [as a supplementary predictor\) linearly. Specifically, when the regression coefficient of \$SVC_{mean}\$](#)
536 [was negative or the fitting efficiency was low \(\$R^2<0.5\$; significance \$p\$ -value \$>0.05\$ \), we excluded](#)
537 [the supplementary predictor from the regression, only exploring the linear relationship between](#)
538 [\$TC_{mean}\$ and AGBC. Afterwards, if the regression between \$TC_{mean}\$ and AGBC was still invalid,](#)
539 [we enlarged the searching window size to \$5\times 5\$, then \$7\times 7\$, and finally \$9\times 9\$, until the regression](#)
540 [as well as the coefficients became valid. Then, the grid annual AGBC from 2002 to 2021 can](#)
541 [be estimated from the TC or both TC and SVC in each year, following the regression results. If](#)
542 [the regression failed even if the window size reached \$9\times 9\$, we stopped expanding the searching](#)

543 [window to avoid the ‘homogeneous assumption’ being invalid. In those grids, following a](#)
544 [previous study \(Xu et al., 2021\), we divided the estimated AGBC by the \$TC_{mean}\$ during 2011–](#)
545 [2015 and then multiplied the TC in each year to obtain the AGBC time series. The above](#)
546 [method utilized spatial information to estimate the temporal variation, and can thus be referred](#)
547 [to as the ‘space for time’ method.](#)

548 [Long-term continuous microwave VOD can also reflect forest biomass changes, although the](#)
549 [relationship was nonlinear \(Jackson and Schmugge, 1991; O’neill et al., 2021; Liu et al., 2015;](#)
550 [Wigneron et al., 1995\). We selected the global land parameter data record \(LPDR\) v3 0.25°](#)
551 [resolution VOD product, which was generated using similar calibrated, X-band brightness](#)
552 [temperature retrieved from the Advanced Microwave Scanning Radiometer \(AMSR-E\) and the](#)
553 [Advanced Microwave Scanning Radiometer 2 \(AMSR2\) \(Du et al., 2017\). As revealed by a](#)
554 [recent evaluation study, LPDR VOD is better correlated with AGB than other long-term VOD](#)
555 [products, especially in less-vegetated areas \(Li et al., 2021\). Because X-band VODs are still](#)
556 [more sensitive to canopy cover than stem biomass and there is a data gap between October 2010](#)
557 [and June 2011, while the plot investigations were all conducted in summers \(Tang et al., 2018\),](#)
558 [we averaged the VOD data from mid-July \(the 206th day\) until the end of September \(the 274th](#)
559 [day\) in each year to represent the annual AGB status. We also aggregated the benchmark AGBC](#)
560 [map as well as the VCF data \(\$TC_{mean}\$ and \$SVC_{mean}\$ \) to 0.25° resolution. After each round of](#)
561 [searching, we applied the shape language modelling algorithm \(D’errico, 2022\) to fit the](#)
562 [nonlinear but monotonous relationship between AGBC and VOD values within the searching](#)

563 [window, and then fitted the bivariate linear regression between AGBC and VCF. If the nonlinear](#)
564 [regression between AGBC and VOD is valid and the \$R^2\$ is superior to the regression between](#)
565 [AGBC and VCF data, LPDR VOD data is expected to outperform VCF in predicting the inter-](#)
566 [annual AGBC changes in the corresponding 0.25° grid. Therefore, in these areas, we calibrated](#)
567 [the VCF-derived high \(1/120°\) resolution annual AGBC by incorporating the ratio between the](#)
568 [VOD-derived 0.25° AGBC and the aggregated VCF-derived AGBC in that year.](#)

569 **[2.3 Forest belowground biomass carbon \(BGBC\) mapping during 2002–2021](#)**

570 [This study mapped belowground forest biomass carbon \(BGBC\) following the random forest](#)
571 [\(RF\) model approach \(Huang et al., 2021\). To reveal forests' above- and belowground biomass](#)
572 [allocation rules in China, this study collated both AGB and BGB records at 8729 forest plots](#)
573 [throughout China, which were obtained using allometric equations or clear-cutting methods](#)
574 [from published papers, including \(Luo, 1996\), \(Luo et al., 2014\), \(Guo and Ren, 2014\), \(Wang](#)
575 [et al., 2014\). Because forest stand age and tree species \(forest type\) information are also](#)
576 [available at 8182 plots, while the climatic backgrounds are available from the WorldClim v2.1](#)
577 [dataset \(Fick and Hijmans, 2017\), forest plots' AGB, forest type \(hereinafter FOR T\), stand](#)
578 [age, mean annual temperature \(MAT\), temperature seasonality \(standard deviation of monthly](#)
579 [temperature×100, abbreviated as Tsea\), mean annual precipitation \(MAP\) and precipitation](#)
580 [seasonality \(coefficient of variation of monthly precipitation, Psea\) were applied as predictors](#)
581 [of forest plots' BGB. For simplicity, we distinguished all forests into 5 types: evergreen](#)

582 [broadleaf forest \(EBF\), deciduous broadleaf forest \(DBF\), evergreen needleleaf forest \(ENF\),](#)
583 [deciduous needleleaf forest \(DNF\), and mixed forest \(MF\). Using the data records at these 8182](#)
584 [plots \(see Figure 2 for the locations of these forest plots and Figure S1c~f for the cumulative](#)
585 [frequency curves and histograms of the AGB and BGB data\), we trained ten-fold RF models](#)
586 [using MATLAB R2021a[®]. The number of regression trees was set to 500.](#)

587 [Because the 1/120° resolution grids where forest AGBC data were available are often mixed](#)
588 [with forestland and some other land cover types, e.g., water bodies, bare ground, croplands, we](#)
589 [converted the annual grid-average AGBC into the AGBC per area forestland by incorporating](#)
590 [the annual fraction of forestland computed from the CLCD at 30 m resolution. Considering the](#)
591 [potential uncertainties in the forestland fraction as well as the inclusion of shrub or herbaceous](#)
592 [plant AGB in the SAR-derived AGB, we only calculated the annual AGBC per area forestland](#)
593 [in grids that were dominated by forestland \(forestland fractions were consistently over 50%\).](#)
594 [In these forestland grids, we simulated the forest BGBC per area forestland during 2002–2021](#)
595 [by inputting the estimated annual AGB \(approximately 2 times of the AGBC\) per forestland,](#)
596 [annual forest type map derived from ESA CCI’s land cover classification dataset \(Li et al.,](#)
597 [2018\), forest stand age \(Besnard et al., 2021\) and climatic background variables into the RF](#)
598 [model. Afterwards, we multiplied the simulation results in every forestland grid with the annual](#)
599 [forestland fractions to obtain the forests’ BGB and BGBC \(0.5×BGB\) time series. Finally, for](#)
600 [grids with forests but are not dominated by forestlands, we sequentially searched for at least](#)
601 [five valid RSR values \(the ratio of forests’ BGBC to AGBC\) nearby \(Chen et al., 2019b\), and](#)

602 [then multiplied the annual forest AGBC in the grid with the median of nearby RSR values in](#)
603 [each year to estimate the annual forest BGBC.](#)

604 **[2.4 Evaluation and assessment](#)**

605 [We compared the inter-annual trend of forest biomass carbon calculated in this study against](#)
606 [that of existing global/regional long-term woody biomass datasets, including the well-received](#)
607 [global long-term terrestrial biomass data between 1993–2012, which was developed mainly](#)
608 [based on a long-term integrated VOD dataset \(Liu et al., 2015\), as well as an updated woody](#)
609 [biomass dataset covering 2001–2019 whose long time series was derived from optical remote](#)
610 [sensing data \(i.e., MODIS VCF dataset\) \(Xu et al., 2021\).](#)

611 [To justify the random forest models for ~~biomass and allocation~~BGBC predictions, we drew](#)
612 [partial dependence plots \(PDPs\) in MATLAB R2021a[®] to show the marginal effect that one](#)
613 [predictor has on the training target \(e.g., BGB at forest plots\)~~from a machine learning model~~](#)
614 [\(~~Hastie et al., 2009~~\)\(Hastie et al., 2009\). Here, for each predictor, we excluded the extreme](#)
615 [values \(the lowest 1% and the highest 1%\) before calculating the corresponding PDP to ~~ensure~~](#)
616 [its robustness~~avoid roughly extending the PDP lines to data-scarce areas~~. Ten-fold RF trainings](#)
617 [were ~~also~~ performed to derive the mean PDP values as well as the standard deviations.](#)

618 **3 Results and discussion**

619 **3.1 ~~Model development and~~ Evaluation of forests' AGBC and BGBC estimation**

620 ~~In the first step, i.e., the benchmark woodland AGB mapping, when ATLAS data derived~~
621 ~~canopy height was applied as an additional predictor in the RF model apart from the three~~
622 ~~biomass datasets (see section 2.1), the number of data points available for training was 1392,~~
623 ~~and the predicted R-square (R^2) according to the ten-fold cross validation was 0.49 ± 0.06 (mean~~
624 ~~\pm standard deviation). The training efficiency is limited by the potential errors in plot-level AGB~~
625 ~~records as well as the CGLS-LC's land cover fraction maps, and the scale difference between~~
626 ~~satellite and plot-level observations. Although introducing climatic and topographic variables~~
627 ~~as predictors could increase the R^2 of ten-fold cross validation, these variables contain high~~
628 ~~spatial autocorrelation, and thus even an elevated R^2 cannot indicate a higher predictive~~
629 ~~performance (Ploton et al. 2020). According to a test addressing the relative contribution of the~~
630 ~~four predictors, GLASS-Biomass dataset contributed most to the woody AGB mapping (35%),~~
631 ~~followed by GlobBiomass (24%), CCI-Biomass (22%) and ATLAS-derived tree volume (19%).~~
632 ~~When GEDI-derived and GLAS-derived wood volumes were respectively used, the available~~
633 ~~data points increased to 3842 and 2286, but the mean R^2 values were both reduced to 0.36. After~~
634 ~~combining these three sets of AGB simulations, the R^2 between the resulting benchmark AGB~~
635 ~~map for China (Figure S1c) and the upscaled plots' AGB was 0.56 (Figure S1b).~~

636 ~~In the second step, i.e., long-term continuous AGB mapping (see section 2.3), with a ten-fold~~

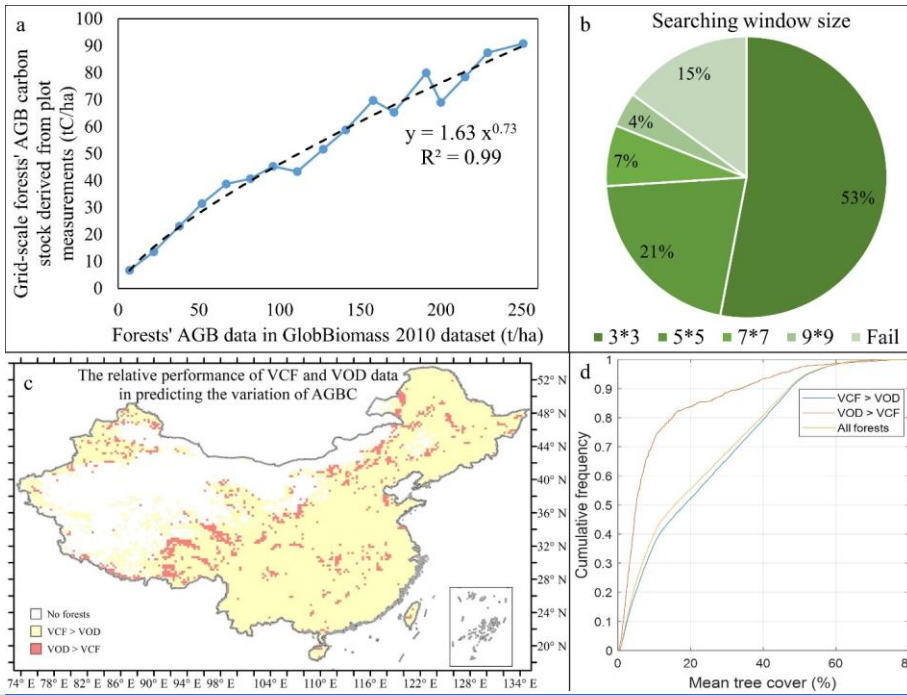
637 cross-validation, the RF model's predictive R^2 and RMSE were 0.79 ± 0.01 and 16.7 ± 0.33 t/ha,
638 respectively. Vegetation continuous fields (VCF) contributed most to the training efficiency
639 (tree cover and all vegetation cover contributed 39% and 17%, respectively). Mean and median
640 vegetation optical depth (VOD) values both contributed 17% to the training efficiency, whereas
641 mean surface soil moisture accounted for 10% (methods are in section 2.3).

642 First, according to Figure 3a, an exponential function: $y=1.63 \times x^{0.73}$ can fit the relationship
643 between the actual grid-scale forest AGBC over 2011–2015 (y) and the AGB values predicted
644 by GlobBiomass 2010 (x). Hence, this function was applied to derive the benchmark map of
645 forest AGBC across China.

646 Second, when using the spatial information of tree cover and short vegetation cover to estimate
647 the temporal variation of AGBC in each grid, the spatial searching window was at its minimum
648 of 3×3 in most (53%) grids with forests. Across China, the temporal extension of AGBC in only
649 15% of all grids with forest cannot be achieved even when the searching window was enlarged
650 to 9×9 (Figure 3b).

651 Next, as shown in Figure 3c and 3d, the grids where LPDR X-band VOD performed better than
652 MODIS VCF in predicting the temporal change in forest AGBC are usually located in regions
653 with low tree cover. These grids account for just 10.4% of all grids with forests, and may suffer
654 from high uncertainty within the optical-based variation in tree cover. Therefore, microwave-
655 based VOD is supposed to be more suitable for estimating the forests' AGBC changes in these

656 [regions.](#)



657
658 [Figure 3. Evaluation of the forest AGBC and BGBC mapping in this study. \(a\) The regression](#)
659 [relationship between the grid-scale forest AGB carbon stock derived from plot measurements](#)
660 [during 2011–2015 and the GlobBiomass AGB dataset for 2010; \(b\) the minimum searching](#)
661 [window sizes of every 1/120° grid when the spatial variation in MODIS VCF was applied as](#)
662 [the predictor of AGBC changes; \(c\) the spatial pattern of the relative performances of MODIS](#)
663 [VCF and LPDR VOD data in predicting the variation in AGBC; \(d\) comparison of the mean](#)
664 [tree cover between the grids where VOD data were more suitable for predicting the variation](#)

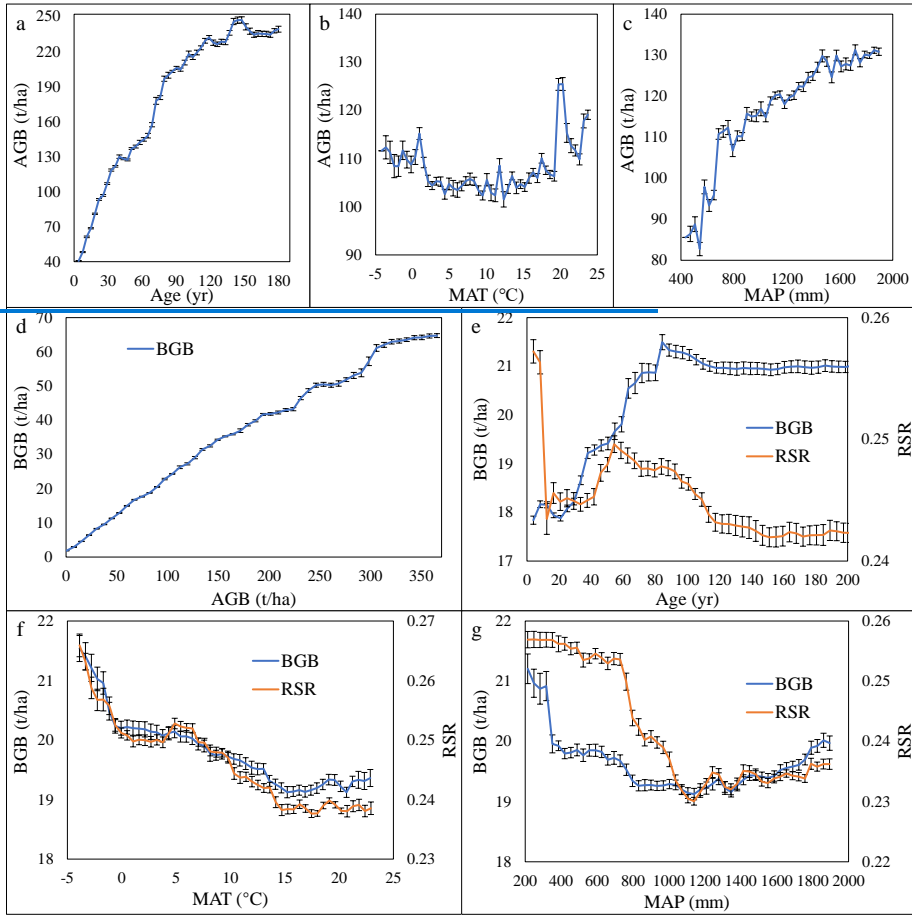
665 [of AGBC and the grids where VCF data were the better predictor.](#)

666 The RF model designed for [woody plots' forest plot](#) BGB estimation (see section 2.53) achieved
667 a predictive R^2 of 0.89 ± 0.02 , while the RMSE was 6.3 ± 0.5 t/ha. AGB explained 53% of the
668 [variation in](#) BGB's [variation](#) among different [woody](#) plots. Long-term climate backgrounds, i.e.,
669 mean annual temperature, temperature seasonality, annual precipitation and precipitation
670 seasonality accounted for 8%, 6%, 8% and 7%, respectively. Forest type and stand age also
671 contributed 12% and 8% to the training efficiency, indicating that the effects of these factors
672 are nonnegligible. The selection of predictors of BGB basically followed the existing
673 knowledge ([Huang et al. 2021](#))([Huang et al., 2021](#)), and the seasonality of temperature and
674 precipitation made sense in the prediction (see Text S1). On the other hand, although previous
675 studies incorporated many edaphic factors as predictors of BGB ([Huang et al. 2021](#)), [by](#)
676 [comparing the training efficiencies when whether these edaphic factors are incorporated](#)([Huang](#)
677 [et al., 2021](#)), [by comparing the training efficiencies when whether these edaphic factors are](#)
678 [incorporated or not](#), we could justify the reasonability of our simplified set of predictors (Text
679 S1).

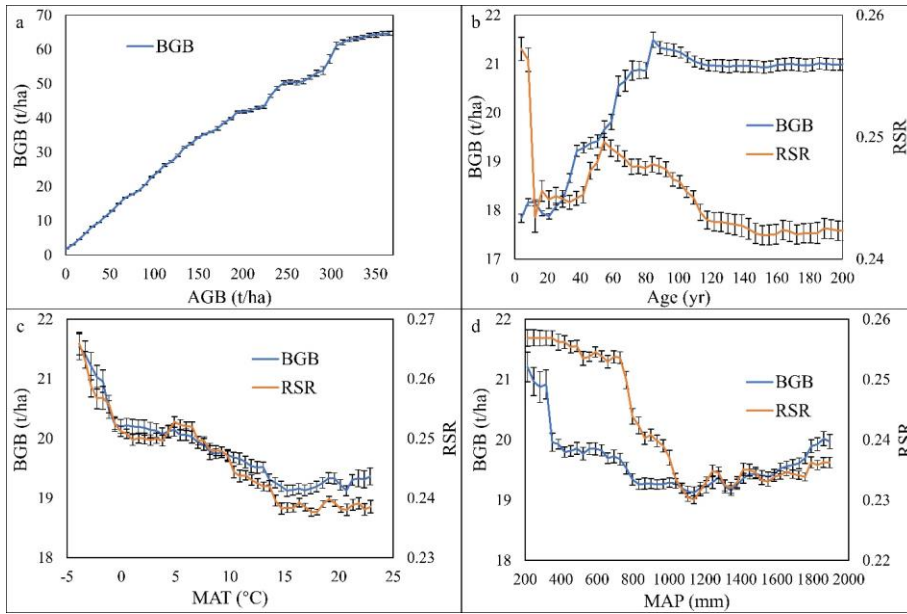
680 ~~We also explored how different factors influence AGB and BGB among woody plots in China.~~
681 ~~Of the biotic and abiotic factors included in our model, partial dependence plots (PDPs, Figure~~
682 ~~2a-c) show that stand age is the main driver of AGB. However, with forest aging, forest growth~~
683 ~~gradually stops, conforming with common knowledge (Xu et al. 2010). Woody AGB also~~

设置了格式: 字体: 倾斜

684 ~~increases significantly with precipitation, but water availability does not constrain biomass in~~
685 ~~humid regions with annual precipitation above 1500 mm, and temperature did not significantly~~
686 ~~affect AGB at large scales. These findings are in line with previous studies (Stegen et al. 2011).~~
687 According to the collected woody plots' data, AGB is a key driver of BGB (Figure ~~2d-g~~4). Yet,
688 RSR changes among different forest growth stages, decreasing in general as reported (~~Mokany~~
689 ~~et al. 2006~~);(~~Mokany et al., 2006~~). The overall negative impact of mean temperature on BGB
690 or RSR agrees with the mechanism that higher heat promotes nutrient accessibility (Luo et al.,
691 2012; Ma et al., 2021), and increases the turnover rates of roots at a higher magnitude than
692 stems (~~Reich et al. 2014~~);(~~Reich et al., 2014~~). The 'U-shaped' relationship between precipitation
693 and belowground biomass allocation follows the 'optimal biomass allocation' theory, because
694 arid climates promote root extension, yet too heavy rainfall reduces nutrient availability through
695 leaching and dilution ~~effect~~effects (Luo et al. 2012);(~~Luo et al., 2012~~). Other factors, including
696 temperature seasonality, precipitation seasonality and forest type, have supplementary effects
697 on ~~the~~ biomass allocation (Figure ~~S8S2~~).



698



699 **Figure 24.** Influence of key factors on woody plots' above and forest belowground woody
700 biomass (BGB) and root-shoot ratio (RSR) in China. Subfigures (a~e) Partial effects of (a)
701 forest age; (b) mean annual temperature (MAT) and (c) mean annual precipitation (MAP) on
702 AGB in all qualified woody plots; (d~g) show partial influences of (a) AGB; (b) stand age; (c)
703 MAT and (d) AGB; (e) stand age; (f) MAT and (g) MAP on BGB and RSR values of all qualified
704 woody forest plots. The error bars represent the standard deviations of the ten-fold trainings. We
705 did not draw the PDP for the impact of AGB on RSR, since the dividend of RSR calculation is
706 AGB.
707

708 3.2 Total woody Forest biomass carbon pool, allocation and change in China

709 Between 2003 to 2020, the total woody biomass in forestlands and shrublands in China were
710 28.4±1.8 Pg and 2.3±0.2 Pg, respectively (Table 1), while the total woody AGB and BGB were
711 24.4±1.6 Pg and 6.2±0.4 Pg. The mean RSR for forests (0.24) and that of all woody areas in

712 China (0.26) are both slightly lower than the global average values of approximately 0.25 and
713 0.3, respectively (Huang et al. 2021; Ma et al. 2021). Separated by forest types, evergreen
714 conifer forest (ENF) occupies the highest woody biomass per unit area (143.5 t/ha), followed
715 by 109.5 t/ha in the evergreen broadleaf forest (EBF), whereas deciduous forests (DBF & DNF)
716 harbor 92 t/ha (Figure 3a). By contrast, deciduous forests in northern China (see Figure S7 for
717 the distribution of forest ecosystems) occupy higher mean RSR values (Figure 3a).

718 Woody biomass across China increased by an average rate of 363.9 ± 11.2 Tg/yr during 2003–
719 2020, equaling a vegetation carbon sink of approximately 163.8 ± 5.9 TgC/yr (assuming a carbon
720 density to biomass ratio of 0.45 (Xu et al. 2018)). Changes in forestland AGB, forestland BGB,
721 shrubland AGB and shrubland BGB account for 73.8%, 7.1%, 15.5% and 3.6%, respectively,
722 of the total woody biomass trend. Apart from visible declines from 2010 to 2011 and from 2016
723 to 2017, China has undergone a continuous increase in woody biomass ($p < 0.01$) during 2003–
724 2020, and the biomass gains were the greatest from 2014 to 2016 (Figure 3b).

725 Our estimates of woody biomass and its trend are generally consistent with previous results in
726 China obtained using both satellite observation and massive field measurements (Table 1). Yet,
727 differences occur in some aspects. For example, as the grass-dominated pixels are excluded in
728 this study, the mean RSR for Chinese shrubs (including those in grass-dominated pixels) was
729 reported as 0.71 (Tang et al. 2018), slightly higher than our estimate of 0.53 for shrubland
730 ecosystems in China. Moreover, regarding trees' occurrence in shrublands, the shrublands'

731 woody biomass and RSR values in this study refer to a mosaic of shrubs and some trees.

732 **Table 1.** Basic statistics of the calculated woody biomass in China and the agreement with those
733 reported previously (the ratio of carbon density to biomass is set to 0.45 (Xu et al. 2018)).

734 Between 2002 to 2021, the forest above- and belowground biomass carbon (AGBC and BGBC)
735 pools in China were 8.6 ± 0.6 and 2.2 ± 0.1 PgC, respectively (Table 1). The mean RSR for all
736 forests was 0.25, basically equal to the global average (Huang et al., 2021). Separated by forest
737 type, evergreen conifer forests (ENF) occupy the highest biomass carbon pool per unit area,
738 mainly because ENF are mainly located in southwestern China and are more mature and natural
739 (Yu et al., 2020; Zhang et al., 2017). Deciduous forests (DBF & DNF) in northern China (see
740 Figure S3 for the distribution of different forest ecosystems) harbor less biomass carbon but
741 higher BGBC (Figure 5a), which can be attributed to the higher RSR values (Table 1).

742 The forest biomass carbon stock in China increased at an average rate of 114.5 ± 16.3 TgC/yr
743 ($p < 0.01$) during 2002–2021, and the annual biomass carbon gains were the greatest from 2014
744 to 2015, reaching 736 TgC (Figure 5b). Changes in AGB and BGB accounted for 81.9% and
745 18.1%, respectively, of the forest carbon stock gains over the past 20 years.

746 Our estimates of the forest biomass carbon pool, forest RSR and the recent inter-annual trend
747 of forest biomass carbon are generally consistent with previous estimates based on massive
748 field investigations (Table 1).

749 **Table 1.** Agreement of the estimated various forest RSR and the trend of forest biomass carbon
750 in China with existing studies.

| Variables related to woody biomass | Our estimate (mean value in 2003–2020) | Previous high-quality estimates | Reference |
|---|--|----------------------------------|---|
| Forestland AGB in China | 22.9 Pg | 18.7 Pg | (Tang et al., 2018) |
| Forestland BGB in China | 5.5 Pg | 4.6 Pg | |
| Shrubland AGB in China | 1.5 Pg | 0.9 Pg | |
| Shrubland BGB in China | 0.8 Pg | 0.7 Pg | (Tang et al., 2018) |
| China Forests' AGBC | 8.6 ± 0.6 (2002–2021) 8.7 ± 0.3 (2011–2015) | 8.4 ± 1.6 (2011–2015) | (Tang et al., 2018; Xu et al., 2018) |
| Woody biomass in China | 30.7 Pg | 24.9–26.4 Pg | (Jiang and Wang, 2017; Tang et al., 2018) |
| Forestland RSR in China | 0.242 ± 0.1 (2002–2021) 2.2 ± 0.1 (2011–2015) | 0.23–0.252 ± 0.4 (2011–2015) | (Tang et al., 2018; Yao et al., 2018) |
| Shrubland RSR in China | 0.53 | 0.71 | |
| ENF's per-area AGB | 143.5 t/ha | ~122 t/ha | (Tang et al., 2018) |
| EBF's per-area AGB | 109.5 t/ha | ~109 t/ha | |
| DBF's per-area AGB | 92.2 t/ha | ~87 t/ha | |
| DNF's per-area AGB | 91.5 t/ha | ~98 t/ha | |
| All forests' per-area AGB | 109.3 t/ha | 99–112 t/ha | |
| Forests' per-area total biomass | 137.3 t/ha | 124–144 t/ha | (Tang et al., 2018; Yao et al., 2018) |
| ENF's EBF's RSR | 0.2227 ± 0.0307 | 0.2422 ± 0.11 | (Tang et al., 2018) |
| EBF's DBF's RSR | 0.2531 ± 0.0405 | 0.2228 ± 0.15 | |
| DBF's ENF's RSR | 0.3022 ± 0.0304 | 0.2824 ± 0.11 | |
| DNF's RSR | 0.3429 ± 0.0410 | 0.31 ± 0.13 | |
| Annual woody forest carbon stock increase | 105.1 ± 42.2 TgC/yr (2002–2010) | 120.2 ± 116.7 TgC/yr (2000–2010) | (Fang et al., 2018) |
| | 163.8 ± 114.5–9 ± 16.3 TgC/yr | 178 TgC/yr (2020–2030) | (Fang et al., 2018) |
| | | 170 TgC/yr (2000s–2040s) | (Yao et al., 2018) |
| Annual forests' carbon stock increase | 146.2–163.8 TgC/yr | 153.6 TgC/yr (2003–2020) | (Qiu et al., 2020) |

格式化表格

格式化表格

合并的单元格

合并的单元格

格式化表格

格式化表格

拆分的单元格

拆分的单元格

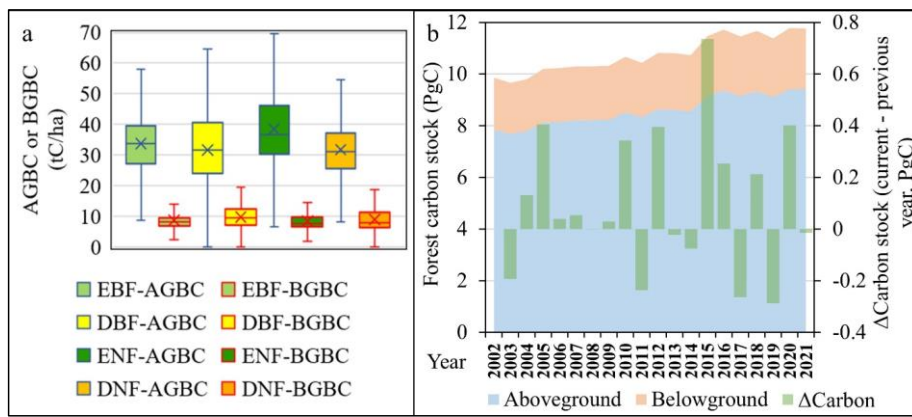
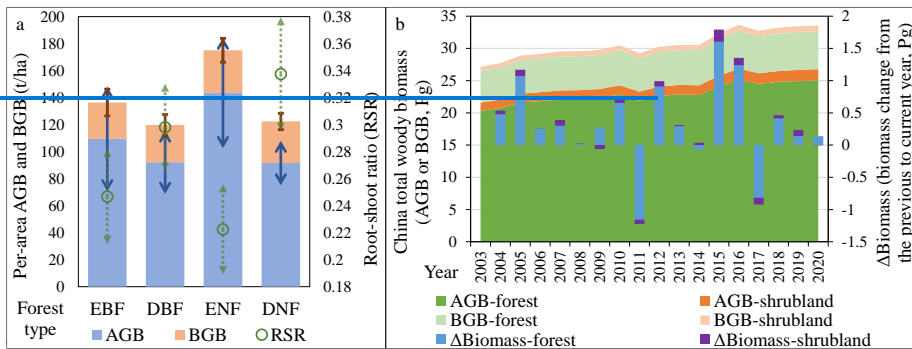
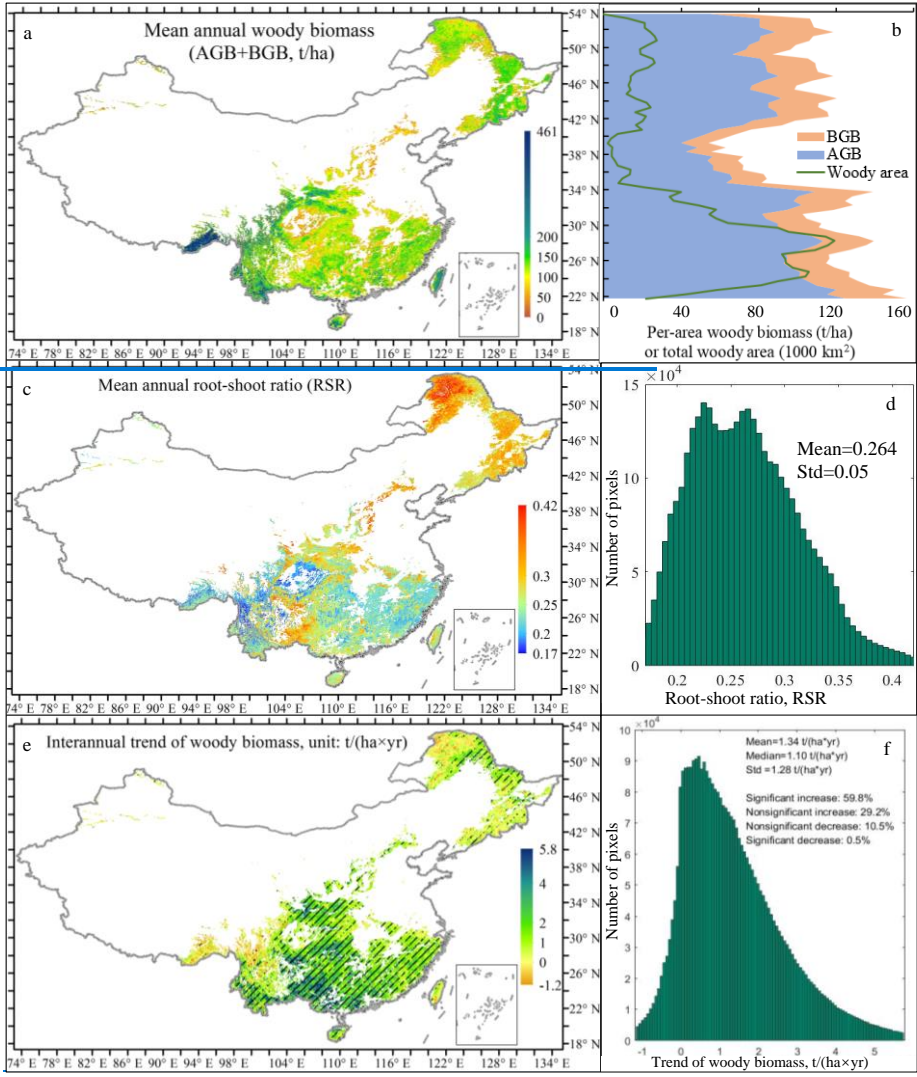


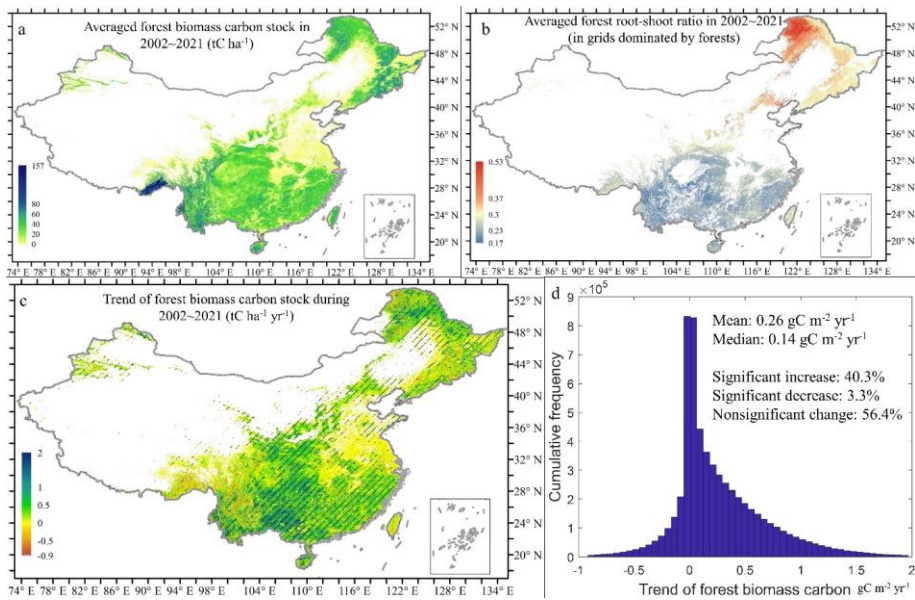
Figure 3. Woody5. Forest biomass allocation and biomass change in China during 2003–2021: (a) per-area AGB and BGB, as well as RSR aboveground biomass carbon (AGBC) and belowground biomass carbon (BGBC) density of different forest ecosystems in China. The blue, red and green error bars are the standard deviations of AGB, BGB and RSR in China; (b) the interannual changes of total forestland' AGB (AGB-forest), shrubland' AGB (AGB-shrubland), forestland' BGB (BGB-AGBC and BGBC in China. Total forest), shrubland' BGB (BGB-shrubland). Biomass biomass carbon stock changes (ΔBiomass) in forests and shrublands from the previous to the current year are represented by blue and purple-green columns.

762 **3.3 ~~Updated spatial hotspots~~Spatial pattern of woody forest biomass amount**
763 **~~and carbon stock~~ trend in China**

764 The highest ~~per-area woodland forest~~ biomass ~~is carbon pools during 2002–2021~~ were observed
765 in ~~the southwest of northeastern and southwestern~~ China, especially ~~south~~southern Tibet.
766 ~~Woody Forest~~ biomass ~~is carbon stocks were~~ also high in ~~parts of the natural or semi-natural~~
767 ~~forests in~~ the Qinling Mountains, Hengduan Mountains, Hainan and Taiwan ~~islands~~ (Figure 4a).
768 Hence, woody biomass was highest in the south < 34°N, followed by the northeast forests, and
769 lowest in the mid-latitudes, 38–40°N (Figure 4b-6a). Above- and belowground ~~woody forest~~
770 biomass allocation varies significantly among regions. RSR is highest in northeastern
771 ~~deciduous~~ conifer forests and northern China's deciduous forest. ~~The southwest karsts also have~~
772 ~~higher RSR than its surroundings due to high shrubland biomass (Figure 4c and Figure S5b).~~
773 ~~Woody pixels' RSR ranges from 0.17 to 0.42 across China, with 67% of pixels having a RSR~~
774 ~~of 0.2–0.3 (Figure 4d).~~ broadleaf forests but low in southern China (Figure 6b). The strongest
775 forest biomass ~~carbon~~ increases were found in central to southern China, including the ~~southern~~
776 ~~part of the~~ Loess Plateau, ~~the~~ Qinling Mountains, ~~the~~ southwest karst region and southeastern
777 forests. ~~Declines~~Slight declines in ~~woody forest~~ biomass ~~carbon~~ only occurred in some mature
778 ~~and~~ natural forests, e.g., those in the Greater Khingan Mountain, Hengduan Mountains and
779 South Tibet (Figure 4e). ~~59.8%~~6c). A total of ~~woody areas~~40.3% of all forests in China showed
780 significant biomass ~~carbon stock~~ gains (Figure 4f over the past 20 years, whereas only 3.3% of
781 ~~forests experienced significant biomass carbon losses (Figure 6d).~~



782



783
 784 **Figure 46.** Maps of woody forest biomass amount carbon pool, allocation and trend in China
 785 during 2003–2020/2002–2021. (a) Spatial pattern of woody total biomass in China; (b) the
 786 latitudinal pattern of per-area woody AGB, BGB and total woody area in China (woody areas
 787 below 22°N are limited); (c–d) map of woody vegetation’s RSR and its histogram; (e–f) map
 788 of the woody biomass trend and its histogram. Shaded areas in trend maps indicate the forest
 789 biomass carbon pool in China; (b) all forestland pixels’ RSR; (c) map of the forest biomass
 790 carbon stock trend from 2002 to 2021, with shaded areas representing statistically significant
 791 trends at the 95% confidence level, while the; (d) histogram and basic statistics of all woody
 792 pixels’ forest biomass amount and carbon stock trend are labelled in the subfigures with
 793 histograms.

794 ~~In agreement with our results (AGB: 24.4 ± 1.6 Pg, total biomass: 30.7 ± 2.0 Pg),~~
795 ~~previous studies estimated a total woody AGB in China of 23.4 ± 0.6 Pg after~~
796 ~~2003 (Liu et al. 2015) and a total woody biomass of 29.4 ± 1.1 Pg during~~
797 ~~2003–2019 (Xu et al. 2021). However, the spatial pattern inferred here~~
798 ~~markedly differ compared with these previous estimates. We predict higher~~
799 ~~woody biomass in the central-south and southwest China but lower biomass~~
800 ~~values in the northern and northwest regions (Figure S9a–f). The spatial~~
801 ~~pattern of our AGB map agrees well with that of recent high-quality China’s~~
802 ~~forest AGB maps which were developed by integrating Lidar, P-band SAR~~
803 ~~and forest inventory data~~ 4 Discussion

804 4.1 Comparison of the estimated forest biomass carbon pool change in this study against 805 the existing datasets

806 Although with potential overestimation, the inter-annual variation in forest AGBC in China
807 according to Liu et al. (2015) and that of total biomass carbon according to Xu et al. (2021) are
808 both highly correlated with our results ($R^2= 0.65$ and 0.88). Liu et al. predicted a forest AGBC
809 increase rate of 102.2 ± 35.8 Tg/yr ($p < 0.01$), slightly higher than our estimate of 80.8 ± 25.1
810 Tg/yr during 2002–2012; while Xu et al. indicated a biomass carbon stock trend of 99.4 ± 23.2
811 Tg/yr ($p < 0.01$) from 2002 to 2019, slightly lower than the rate of 115.6 ± 20.2 Tg/yr in this
812 study (Figure 7a~b). The spatial maps of the forest biomass carbon trends estimated by Xu et

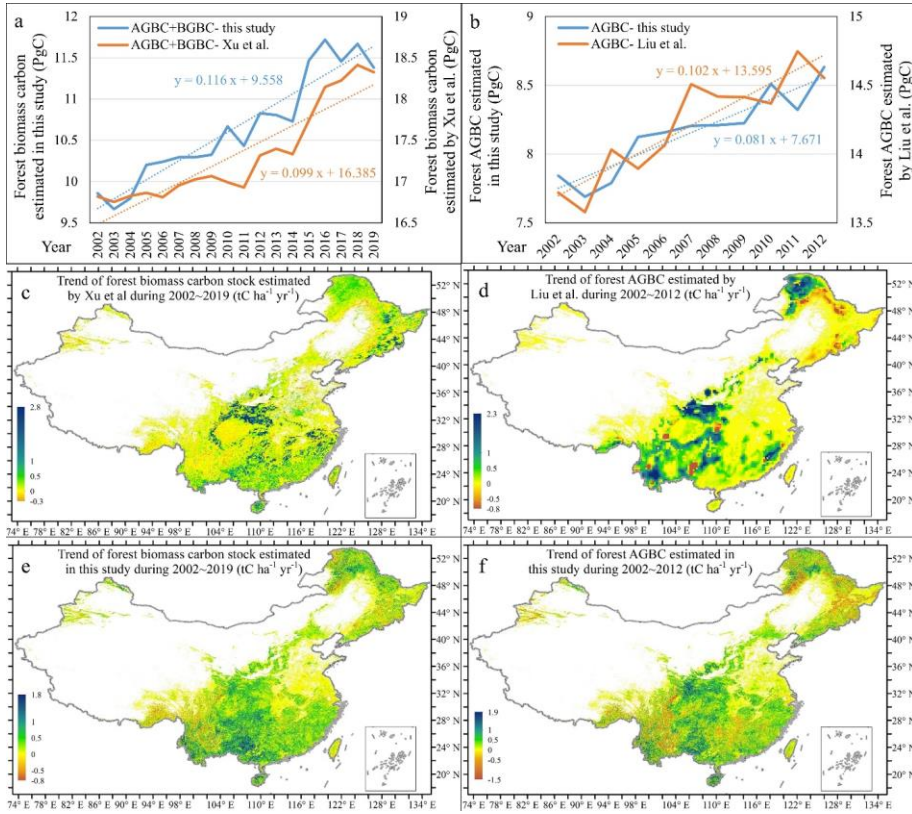
813 al. and Liu et al. were slightly patchy (Figure 7c~d). Compared to this study, the two existing
814 datasets (i.e., Liu et al. (2015) and Xu et al. (2021)'s datasets) predicted higher biomass carbon
815 stock trends in the Qinling Mountains and the mature deciduous conifer forests in northeast
816 China. Meanwhile, they predicted lower carbon sinks in southern China (Figure 7c~f), where
817 reforestation and forest management-induced short term extensive carbon uptake (Tong et al.,
818 2020) have been confirmed by atmospheric inversions (Wang et al., 2020; Yang et al., 2021).
819 Finally, by comparing Figure 7e and 7f, we could also notice that the hotspot of forest biomass
820 carbon gains has moved from the Loess Plateau over the first decade of our study period (2002–
821 2012) to southern China (e.g., Guangxi Province) later. This change was probably due to the
822 large-scale implementation of the 'Grain for Green' project on the Loess Plateau (HuangLiu et
823 al. 2019; Su., 2020; Wu et al. 2016., 2019), with the correlation coefficients both reaching 0.73.
824 For Liu et al. (2015)'s and Xu et al. (2021)'s dataset, the spatial pattern correlations with those
825 improved AGB maps are 0.35–0.50 and 0.27–0.37, respectively (Figure S10). The average
826 woody AGB in eight provinces of southern China was 92–104 t/ha (Tong et al. 2020), close to
827 our estimate of 85–110 t/ha. Forest inventory indicated a tree biomass of 1.92 Pg in Tibet (Sun
828 et al. 2016) where our result was 1.86 Pg yet the two existing long-term datasets predicted
829 1.26–1.52 Pg.
830 The interannual variation in woody AGB in China according to Liu et al. (2015) and that of
831 total woody biomass according to Xu et al. (2021) are both highly correlated with our results

设置了格式

832 ($r=0.76$ and 0.95). Liu et al. predicted a woody AGB increasing rate of 186 ± 79.6 Tg/yr ($p<0.01$);
833 similar to our estimate of 236 ± 117 Tg/yr during 2003–2012; while Xu et al. indicated a biomass
834 trend of 219.4 ± 79.6 Tg/yr ($p<0.01$) from 2003 to 2019, lower than the rate of 368 ± 69.9 Tg/yr
835 in this study (Figure S11a, c). Spatially, this study predicted an obviously faster biomass
836 increases in southern China than their datasets (Figure S11). Reforestation and forest
837 management led to a short term extensive carbon sequestration in southern China, which was
838 estimated as 220 ± 100 Tg AGB/yr during 2002–2017 by developing a regional RF model
839 between MODIS reflectance data and a global benchmark AGB map (Tong et al. 2020), close
840 to our estimate of 200 ± 58 Tg AGB/yr. The high ecosystem carbon sink in central to south China
841 and southwestern China has been shown by atmospheric inversions as well (Wang et al. 2020;
842 Yang et al. 2021).

843 Accordingly, by fusing low frequency active, passive microwaves and the advanced LiDAR-
844 derived canopy heights under the reference of extensive field measurements, this study could
845 generate updated estimates on the spatial hotspots of woody biomass and its trends in China.

846 3.4 Uncertainties of the woody biomass dataset— before 2012, and the massive plantation of
847 fast-growing trees in southern China after 2010 (Tong et al., 2020).



848
 849 [Figure 7. Comparison of the estimated forest biomass carbon pool change in this study against](#)
 850 [two existing datasets. \(a\) Comparison of the inter-annual variation of forest biomass carbon in](#)
 851 [this study against the estimate by Xu et al. during 2002–2019; \(b\) comparison of the inter-](#)
 852 [annual variation of forest AGBC calculated in this study against the estimate by Liu et al. over](#)
 853 [2002–2012; \(c\) map of the inter-annual trend of forest biomass carbon stock in China during](#)
 854 [2003–2019 according to Xu et al; \(d\) map of the forest AGBC trend in China during 2003–2012](#)
 855 [according to Liu et al; \(e\) map of the estimated trend of forest biomass carbon stock over 2002–](#)

2019 in this study; (f) map of the estimated forest AGBC trend over 2002–2012 in this study.

4.2 Some uncertainties of the forest biomass carbon dataset and future prospects

The uncertainties of AGB in this study came from four sources: 1) the improved benchmark AGB map for China; 2) the extension of AGB time series based on the long-term integrated VOD and high/short vegetation coverage datasets; 3) downscaling of coarse resolution AGB; and 4) the AGB decomposition process. The uncertainty in BGB was composed of the error within the AGB time series and the prediction uncertainty of the models that transform AGB to BGB. The details for the calculation of each source of error are in Text S2. Finally, the annual AGB and BGB's relative error can be calculated as the square root of the sum of squares of all relative errors, which is referred to as the 'error propagation rule' when assuming that each error is independent and random (Huang et al. 2021). By multiplying the annual AGB or BGB map with the corresponding relative error, we mapped the AGB and BGB's uncertainties in China annually during 2003–2020. As shown in Figure S12, the spatial patterns of the relative errors of AGB and BGB are similar. Relative errors were lower in the pure forests located in northeast China and the south Tibet, and high in the mixed forest and shrublands in the southwest karst regions and part of North China.

A recent study revealed that the variation in VODs is correlated with not only biomass, but also soil moisture availability (Konings et al. 2021). To alleviate this source of uncertainty as much as possible, we have incorporated the satellite-based surface soil moisture dataset to account

875 for the impact from the interannual variation in water content per biomass. In addition, we have
876 included optical based vegetation continuous fields in predicting the spatiotemporal variation
877 in biomass, which turned out to be the variable with the highest contribution (56%). In fact, the
878 interannual variation in Chinese woody biomass according to this study is highly correlated
879 ($r=0.95$) with that calculated independent of microwave based VOD (Xu et al. 2021).

880 Next, the During benchmark AGBC mapping, we converted the in-situ AGBC data at forest
881 plots into the grid-scale average AGBC by multiplying by the fraction of forestland during the
882 time period of field investigation. Considering the overall high-quality of the China's land-
883 use/cover datasets developed via human-computer interactive interpretation of Landsat images
884 (Liu et al., 2014; Yang and Huang, 2021), and that the producer's accuracy (PA) and user's
885 accuracy (UA) for forestland classification in the CLCD dataset used in this study were 73%
886 and 85% respectively, the errors within the benchmark AGBC mapping induced by the scale
887 conversion based on the forestland area fraction were generally limited.

888 The variation in climatic conditions in atthe short term may have subtle influences on that in the
889 BGB, but explicit knowledge on this effect is lacking. Instead, woody vegetation BGB is much
890 more driven by AGB (vegetation density), as indicated by the very strong relationship between
891 BGB and AGB ($R^2 \geq 0.85$). Moreover, the long-term climatic background is expected to have a
892 stronger influence on the RSR of perennial woody plants than the meteorological conditions in
893 only a few years, since above- and belowground biomass allocation is the result of plants' long-

设置了格式: 字体: 倾斜

894 term adjustment to the environment ([Qi et al. 2019](#)). Accordingly ([Qi et al., 2019](#)). Therefore, it
895 is reasonable not to consider the influence of the specific climatic conditions in a year on the
896 variation in BGB.

897 In [the](#) near future, P-band microwave sensors, which have higher penetrability into the canopy
898 than L-band microwaves, will further improve ~~the~~ AGB mapping. For example, BIOMASS, a
899 fully polarimetric P-band SAR, is scheduled to be launched in 2022 (~~Le Toan et al. 2011~~)([Le
900 Toan et al., 2011](#)). Therefore, in the future the relationship between P-band microwave retrievals
901 and biomass should be addressed, as well as the calibration of historical AGB datasets (e.g., the
902 long-term AGB dataset in this study) against the P-band SAR-based AGB benchmark map to
903 extend the time series. [In addition, an inter-calibration between the AMSR-E-based VOD and
904 the AMSR2-based VOD will further reduce the potential bias within the long-term integrated
905 VOD datasets \(Wang et al., 2021a; Wang et al., 2021b\)](#). On the other hand, more in-situ AGB
906 and BGB measurements in larger plots are needed to further improve the estimation of
907 belowground biomass allocation.

908 **Data availability**

909 [Annual forest above- and belowground biomass maps in China between 2002 and 2021 are now
910 available at: <https://doi.org/10.6084/m9.figshare.21931161.v1>. This dataset will also be
911 available on the National Tibetan Plateau/Third Pole Environment Data Center and PANGAEA
912 soon \(under checking now\). Annual AGB and BGB in China will be available on the National](#)

~~Tibetan Plateau/Third Pole Environment Data Center and PANGAEA~~: Other open datasets that made this research possible and the related references are attached in Supplementary Information- Text [S3S2](#).

Funding and acknowledgements

This work was supported by the ~~National Key~~[CAS Project for Young Scientists in Basic Research and Development Program of China \(2017YFA0604700\)](#), ~~National Science Foundation of China (41991233)~~ and the Chinese Academy of Sciences (~~QYZDY-SSW-DQC025~~), [\(YSBR-037\)](#). We are grateful to all the data contributors, especially [Yuan Zhang Xuli Tang for sharing in-situ measurements of forest aboveground biomass carbon stock across China](#), and Huabing Huang for sharing ~~the forest stand age map and his~~ forest aboveground biomass map ~~in China to us~~.

Conflict of interests

The authors declare no conflict of interest.

Credit author statement

Y.C designed and conducted the research. B.F and X.F funded the research. Y.Z wrote the draft of the manuscript; X.F and all other authors read and revised the manuscript.

References

- [Baret, F., Weiss, M., Lacaze, R., Camacho, F., Makhmara, H., Pacholezyk, P., & Smets, B. \(2013\). GEOV1: LAI and FAPAR essential climate variables and FCOVER global time-series capitalizing over existing products. Part I: Principles of development and production. Remote. Sens. Environ., 137, 299–309](#)
- [Besnard, S., Koirala, S., Santoro, M., Weber, U., Nelson, J., Gütter, J., Herault, B., Kassi, J., N'Guessan, A., Neigh, C., Poulter, B., Zhang, T., and Carvalhais, N.: Mapping global forest age from forest inventories, biomass and climate data. Earth Syst. Sci. Data, 13, 4881–4896. <https://doi.org/10.5194/essd-13-4881-2021>, 2021.](#)

936 Bouvet, A., Mermoz, S., Le Toan, T., Villard, L., Mathieu, R., Naidoo, L., & Asner, G. P. (2018). An above-
937 ground biomass map of African savannahs and woodlands at 25m resolution derived from ALOS PALSAR-
938 Remote Sens. Environ., 206, 156-173, <https://doi.org/10.1016/j.rse.2017.12.030>, 2018.

939 Buehner, M., Lesiv, M., Tsendbazar, N. E., Herold, M., Bertels, L., & Smets, B. (2020). Copernicus Global Land
940 Cover Layers—Collection 2. Remote Sens., 12

941 Cammalleri, C., Verger, A., Lacaze, R., & Vogt, J.V. (2019). Harmonization of GEOV2 fAPAR time-series through
942 MODIS data for global drought monitoring. Int. J. Appl. Earth Obs., 80, 1-12

943 Cartus, O., Santoro, M., & Kellndorfer, J. (2012). Mapping forest aboveground biomass in the Northeastern
944 United States with ALOS PALSAR dual-polarization L-band. Remote Sens. Environ., 124, 466-478,
945 <https://doi.org/10.1016/j.rse.2012.05.029>, 2012.

946 Chang, Z., Hobeichi, S., Wang, Y.-P., Tang, X., Abramowitz, G., Chen, Y., Cao, N., Yu, M., Huang, H., Zhou, G.,
947 Wang, G., Ma, K., Du, S., Li, S., Han, S., Ma, Y., Wigner, J.-P., Fan, L., Saatchi, S. S., and Yan, J.: New Forest
948 Aboveground Biomass Maps of China Integrating Multiple Datasets, Remote Sens., 13,
949 <https://doi.org/10.3390/rs13152892>, 2021.

950 Chen, C., Park, T., Wang, X., Piao, S., Xu, B., Chaturvedi, R. K., Fuchs, R., Brovkin, V., Ciais, P., Fensholt, R.,
951 Tommervik, H., Bala, G., Zhu, Z., Nemani, R. R., & Myneni, R. B. (2019a). China and India lead in greening
952 of the world through land-use management. Nat. Sustain., 2, 122-129,
953 <https://doi.org/10.1029/2018EF00089010.1038/s41893-019-0220-7>, 2019a.

954 Chen, Y., Feng, X., & Fu, B. (2021). An improved global remote sensing-based surface soil moisture (RSSM)
955 dataset covering 2003–2018. Earth Syst. Sci. Data, 13, 1-31

956 Chen, Y., Feng, X., Fu, B., Shi, W., Yin, L., & Lv, Y. (2019b). Recent Global Cropland Water Consumption
957 Constrained by Observations. Water Resour. Res., 55, 3708-3738, <http://doi.org/10.1029/2018WR023573>, 2019b.

958 Dubayah, R., Blair, J.B., Goetz, S., Fatoyinbo, L., Hansen, M., Healey, S., Hofton, M., Hurtt, G., Kellner, J.,
959 Luthcke, S., Armston, J., Tang, H., Duncanson, L., Hancock, S., Jantz, P., Marselis, S., Patterson, P.L., Qi, W., &
960 Silva, C. (2020). The Global Ecosystem Dynamics Investigation: High-resolution laser ranging of the Earth's
961 forests and topography. Sci. Remote Sens., 1, 100002

962 D'Errico, J.: SLM - Shape Language Modeling MATLAB Central File Exchange [code], 2022.

963 DiMiceli, C., Sohlberg, R., and Townshend, J.: MODIS/Terra Vegetation Continuous Fields Yearly L3 Global
964 250m SIN Grid V061. [dataset], <https://doi.org/10.5067/MODIS/MOD44B.061>, 2022.

965 Du, J., Kimball, J. S., Jones, L. A., Kim, Y., Glassy, J., and Watts, J. D.: A global satellite environmental data record
966 derived from AMSR-E and AMSR2 microwave Earth observations, Earth Syst. Sci. Data, 9, 791-808,
967 <https://doi.org/10.5194/essd-9-791-2017>, 2017.

968 Enquist Brian, J., & Niklas Karl, J. (2002). Global Allocation Rules for Patterns of Biomass Partitioning in
969 Seed Plants. Science, 295, 1517-1520, <https://doi.org/10.1029/2018EF00089010.1126/science.1066360>, 2002.

970 Fang, J., Yu, G., Liu, L., Hu, S., & Chapin, F. S. (2018). Climate change, human impacts, and carbon

带格式的: 段落间距段前: 8.15 磅, 段后: 0 磅

带格式的: 段落间距段前: 8.15 磅, 段后: 0 磅

带格式的: 段落间距段前: 8.15 磅, 段后: 0 磅

带格式的: 段落间距段前: 8.15 磅, 段后: 0 磅

带格式的: 段落间距段前: 8.15 磅, 段后: 0 磅

971 sequestration in China. *P. Natl. Acad. Sci. USA*, 115, 4015,
972 <https://doi.org/10.1029/2018EF00089010.1073/pnas.1700304115>, 2018.

973 Fick, S. E., & Hijmans, R. J. (2017). WorldClim 2: new 1-km spatial resolution climate surfaces for global
974 land areas. *Int. J. Climatol.*, 37, 4302-4315, <https://doi.org/10.1029/2018EF00089010.1002/joc.5086>, 2017.

975 Frappart, F., Wigneron, J.-P., Li, X., Liu, X., Al-Yaari, A., Fan, L., Wang, M., Moisy, C., Le Masson, E., Aoulad
976 Lafkih, Z., Vallé, C., Ygorra, B., & Baghdadi, N. (2020). Global Monitoring of the Vegetation Dynamics from
977 the Vegetation Optical Depth (VOD): A Review. *Remote Sens.*, 12,
978 <https://doi.org/10.1029/2018EF00089010.3390/rs12182915>, 2020.

979 Guo, J., Guo, Y., Chai, Y., Liu, X., & Yue, M. (2021). Shrubland biomass and root-shoot allocation along a climate
980 gradient in China. *Plant Ecol. Evol.*, 154, 5-14

981 Guo, Q., & Ren, H. (2014). Productivity as related to diversity and age in planted versus natural forests. *Global Ecol. Biogeogr.*, 23, 1461-1471, <https://doi.org/10.1111/geb.12238>, 2014.

983 Hansen, M. C., Potapov, P. V., Moore, R., Hancher, M., Turbanova, S. A., Tyukavina, A., Thau, D., Stehman, S.
984 V., Goetz, S. J., Loveland, T. R., Kommareddy, A., Egorov, A., Chini, L., Justice, C. O., and Townshend, J. R. G.:
985 High-Resolution Global Maps of 21st-Century Forest Cover Change. *Science*, 342, 850-853,
986 <https://doi.org/10.1126/science.1244693>, 2013.

987 Hastie, T., Tibshirani, R., & Friedman, J. (2009). The Elements of Statistical Learning Data Mining, Inference,
988 and Prediction, Second Edition, Section 10.13.2. Springer, Springer 2009.

989 Hu, T., Su, Y., Xue, B., Liu, J., Zhao, X., Fang, J., & Guo, Q. (2016). Mapping Global Forest Aboveground
990 Biomass with Spaceborne LiDAR, Optical Imagery, and Forest Inventory Data. *Remote Sens.*, 8, [Remote Sens.,
991 8, <https://doi.org/10.1029/2018EF00089010.3390/rs8070565>, 2016.](https://doi.org/10.1029/2018EF00089010.3390/rs8070565)

992 Huang, H., Liu, C., Wang, X., Zhou, X., & Gong, P. (2019). Integration of multi-resource remotely sensed
993 data and allometric models for forest aboveground biomass estimation in China. *Remote Sens. Environ.*, 221,
994 225-234, <https://doi.org/10.1016/j.rse.2018.11.017>, 2019.

995 Huang, Y., Ciais, P., Santoro, M., Makowski, D., Chave, J., Schepaschenko, D., Abramoff, R. Z., Goll, D. S., Yang,
996 H., Chen, Y., Wei, W., & Piao, S. (2021). A global map of root biomass across the world's forests. *Earth Syst.*
997 *Sci. Data*, 13, 4263-4274, <https://doi.org/10.1029/2018EF00089010.5194/essd-13-4263-2021>, 2021.

998 Jackson, T. J., & Schmugge, T. J. (1991). Vegetation effects on the microwave emission of soils. *Remote.*
999 *Sens. Environ.*, 36, 203-212, [https://doi.org/10.1016/0034-4257\(91\)90057-D](https://doi.org/10.1016/0034-4257(91)90057-D), 1991.

1000 Jiang, Y., & Wang, L. (2017). Pattern and control of biomass allocation across global forest ecosystems. *Ecol.*
1001 *Evol.*, 7, 5493-5501

1002 Konings, A.G., Holtzman, N.M., Rao, K., Xu, L., & Saatchi, S.S. (2021). Interannual Variations of Vegetation
1003 Optical Depth are Due to Both Water Stress and Biomass Changes. *Geophys. Res. Lett.*, 48, e2021GL095267

1004 Konings, A.G., Piles, M., Das, N., & Entekhabi, D. (2017). L-band vegetation optical depth and effective scattering
1005 albedo estimation from SMAP. *Remote Sens. Environ.*, 198, 460-470

带格式的: 段落间距段前: 8.15 磅, 段后: 0 磅

带格式的: 段落间距段前: 8.15 磅, 段后: 0 磅

1006 Kumar, L., & Mutanga, O. (2017). Remote Sensing of Above-Ground Biomass. *Remote Sens.*, 9, <https://doi.org/10.1029/2018EF00089010.3390/rs9090935>, 2017.

1007

1008 Le Toan, T., Quegan, S., Davidson, M. W. J., Balzter, H., Paillou, P., Papathanassiou, K., Plummer, S., Rocca, F.,
 1009 Saatchi, S., Shugart, H., & Ulander, L. (2011). The BIOMASS mission: Mapping global forest biomass to
 1010 better understand the terrestrial carbon cycle. *Remote. Sens. Environ.*, 115, 2850-2860,
 1011 <https://doi.org/10.1016/j.rse.2011.03.020>, 2011.

1012 Leys, C., Ley, C., Klein, O., Bernard, P., & Licata, L. (2013). Detecting outliers: Do not use standard deviation
 1013 around the mean, use absolute deviation around the median. *J. Exp. Soc. Psychol.*, 49, 764-766

1014 Li, W., MacBean, N., Ciais, P., Defourny, P., Lamarche, C., Bontemps, S., Houghton, R. A., & Peng, S. (2018).
 1015 Gross and net land cover changes in the main plant functional types derived from the annual ESA CCI land cover
 1016 maps (1992–2015). *Earth Syst. Sci. Data*, 10, 219-234, [https://doi.org/10.1029/2018EF00089010.5194/essd-10-](https://doi.org/10.1029/2018EF00089010.5194/essd-10-219-2018)
 1017 [219-2018](https://doi.org/10.1029/2018EF00089010.5194/essd-10-219-2018), 2018.

1018 Li, X., Wigneron, J.-P., Frappart, F., Fan, L., Ciais, P., Fensholt, R., Entekhabi, D., Brandt, M., Konings, A. G.,
 1019 Liu, X., Wang, M., Al-Yaari, A., & Moisy, C. (2021). Global-scale assessment and inter-comparison of
 1020 recently developed/reprocessed microwave satellite vegetation optical depth products. *Remote. Sens. Environ.*,
 1021 253, 112208, <https://doi.org/10.1016/j.rse.2020.112208>, 2021.

1022 Liu, M., Li, D., Hu, J., Liu, D., Ma, Z., Cheng, X., Zhao, C., & Liu, Q. (2020). Altitudinal pattern of shrub biomass
 1023 allocation in Southwest China. *PLoS One*, 15, e0240864

1024 Liu, J., Kuang, W., Zhang, Z., Xu, X., Qin, Y., Ning, J., Zhou, W., Zhang, S., Li, R., Yan, C., Wu, S., Shi, X., Jiang,
 1025 N., Yu, D., Pan, X., and Chi, W.: Spatiotemporal characteristics, patterns and causes of land use changes in China
 1026 since the late 1980s, *Dili Xuebao/Acta Geogr. Sin.*, 69, 3-14, <https://doi.org/10.11821/dlxb201401001>, 2014.

1027 Liu, X., Su, Y., Hu, T., Yang, Q., Liu, B., Deng, Y., Tang, H., Tang, Z., Fang, J., & Guo, Q. (2022). Neural
 1028 network guided interpolation for mapping canopy height of China's forests by integrating GEDI and ICESat-2
 1029 data. *Remote. Sens. Environ.*, 269, 112844, <https://doi.org/10.1016/j.rse.2021.112844>, 2022.

1030 Liu, Y. Y., de Jeu, R. A. M., McCabe, M. F., Evans, J. P., & van Dijk, A. I. J. M. (2011). Global long-term
 1031 passive microwave satellite-based retrievals of vegetation optical depth. *Geophys. Res. Lett.*, 38,
 1032 <https://doi.org/10.1029/2011GL048684>, 2011.

1033 Liu, Y. Y., van Dijk, A. I. J. M., de Jeu, R. A. M., Canadell, J. G., McCabe, M. F., Evans, J. P., & Wang, G.
 1034 (2015). Recent reversal in loss of global terrestrial biomass. *Nat. Clim. Change*, 5, 470-474,
 1035 <https://doi.org/10.1029/2018EF00089010.1038/nclimate2581>, 2015.

1036 Liu, Z., Wang, J., Wang, X., and Wang, Y.: Understanding the impacts of 'Grain for Green' land management
 1037 practice on land greening dynamics over the Loess Plateau of China, *Land Use Policy*, 99, 105084,
 1038 <https://doi.org/10.1016/j.landusepol.2020.105084>, 2020.

1039 Lu, F., Hu, H., Sun, W., Zhu, J., Liu, G., Zhou, W., Zhang, Q., Shi, P., Liu, X., Wu, X., Zhang, L., Wei, X., Dai, L.,
 1040 Zhang, K., Sun, Y., Xue, S., Zhang, W., Xiong, D., Deng, L., Liu, B., Zhou, L., Zhang, C., Zheng, X., Cao, J.,

带格式的: 段落间距段前: 8.15 磅, 段后: 0 磅

带格式的: 段落间距段前: 8.15 磅, 段后: 0 磅

带格式的: 段落间距段前: 8.15 磅, 段后: 0 磅

带格式的: 段落间距段前: 8.15 磅, 段后: 0 磅

1041 Huang, Y., He, N., Zhou, G., Bai, Y., Xie, Z., Tang, Z., Wu, B., Fang, J., Liu, G., & Yu, G. (2018). Effects of
1042 national ecological restoration projects on carbon sequestration in China from 2001 to 2010. *P. Natl. Acad. Sci.*
1043 *USA*, 115, 4039-4044. <https://doi.org/10.1029/2018EF000890>.
1044 Luo, T. (1996). Patterns of net primary productivity for Chinese major forest types and their mathematical models.
1045 *Chinese Academy of Sciences*, 1996.
1046 Luo, Y., Zhang, X., Wang, X., and Lu, F.: Biomass and its allocation of Chinese forest ecosystems. *Ecology*, 95,
1047 2026-2026. <https://doi.org/10.1890/13-2089.1>, 2014.
1048 Luo, Y., Wang, X., Zhang, X., Booth, T. H., & Lu, F. (2012). Root:shoot ratios across China's forests: Forest
1049 type and climatic effects. *Forest Ecol. Manag.*, 269, 19-25. <https://doi.org/10.1016/j.foreco.2012.01.005>, 2012.
1050 Luo, Y., Zhang, X., Wang, X., & Lu, F. (2014). Biomass and its allocation of Chinese forest ecosystems. *Ecology*,
1051 95, 2026-2026
1052 Ma, H., Mo, L., Crowther, T. W., Maynard, D. S., van den Hoogen, J., Stocker, B. D., Terrer, C., & Zohner, C.
1053 M. (2021). The global distribution and environmental drivers of aboveground versus belowground plant biomass.
1054 *Nat. Ecol. Evol.*, <https://doi.org/10.1038/s41559-021-01485-1>, 2021.
1055 Markus, T., Neumann, T., Martino, A., Abdalati, W., Brunt, K., Csatho, B., Farrell, S., Fricker, H., Gardner, A.,
1056 Harding, D., Jasinski, M., Kwok, R., Magruder, L., Lubin, D., Luthcke, S., Morison, J., Nelson, R.,
1057 Neuenschwander, A., Palm, S., Popescu, S., Shum, C.K., Schutz, B.E., Smith, B., Yang, Y., & Zwally, J. (2017).
1058 The Ice, Cloud, and land Elevation Satellite 2 (ICESat-2): Science requirements, concept, and implementation.
1059 *Remote. Sens. Environ.*, 190, 260-273
1060 Menenti, M., Azzali, S., Verhoef, W., & van Swol, R. (1993). Mapping agroecological zones and time lag in
1061 vegetation growth by means of fourier analysis of time series of NDVI images. *Advances in Space Research*, 13,
1062 233-237
1063 Mialon, A., Rodríguez-Fernández, N. J., Santoro, M., Saatchi, S., Mermoz, S., Bousquet, E., & Kerr, Y. H.
1064 (2020). Evaluation of the Sensitivity of SMOS L-VOD to Forest Above-Ground Biomass at Global Scale.
1065 *Remote Sens.*, 12, 1450. <https://doi.org/10.3390/rs12091450>, 2020.
1066 Moesinger, L., Dorigo, W., de Jeu, R., van der Schalie, R., Scanlon, T., Teubner, I., & Forkel, M. (2020). The global
1067 long-term microwave Vegetation Optical Depth Climate Archive (VODCA). *Earth Syst. Sci. Data*, 12, 177-196
1068 Mokany, K., Raison, R. J., & Prokushkin, A. S. (2006). Critical analysis of root: shoot ratios in terrestrial
1069 biomes. *Global Change Biol.*, 12, 84-96. <https://doi.org/10.1111/j.1365-2486.2005.001043.x>, 2006.
1070 Neuenschwander, A., Guenther, E., White, J.C., Duncanson, L., & Montesano, P. (2020). Validation of ICESat-2
1071 terrain and canopy heights in boreal forests. *Remote. Sens. Environ.*, 251, 112110
1072 Nie, X., Yang, Y., Yang, L., & Zhou, G. (2016). Above and Belowground Biomass Allocation in Shrub Biomes
1073 across the Northeast Tibetan Plateau. *PLoS One*, 11, e0154251
1074 Niu, Q., Xiao, X., Zhang, Y., Qin, Y., Dang, X., Wang, J., Zou, Z., Doughty, R. B., Brandt, M., Tong, X., Horion,
1075 S., Fensholt, R., Chen, C., Myneni, R. B., Xu, W., Di, G., & Zhou, X. (2019). Ecological engineering projects
1076 increased vegetation cover, production, and biomass in semiarid and subhumid Northern China. *Land Degrad.*

带格式的: 段落间距段前: 8.15 磅, 段后: 0 磅

带格式的: 段落间距段前: 8.15 磅, 段后: 0 磅

带格式的: 段落间距段前: 8.15 磅, 段后: 0 磅

带格式的: 段落间距段前: 8.15 磅, 段后: 0 磅

带格式的: 段落间距段前: 8.15 磅, 段后: 0 磅

1077 Dev., 30, 1620-1631, <https://doi.org/10.1002/ldr.3351>, 2019.

1078 O'Neill, P. E., Chan, S., Njoku, E. G., Jackson, T., Bindlish, R., & Chaubell, J. (2021). SMAP Enhanced L3
 1079 Radiometer Global Daily 9 km EASE-Grid Soil Moisture, Version 5. In Boulder, Colorado USA. NASA
 1080 National Snow and Ice Data Center Distributed Active Archive Center. [\[dataset\]](#),
 1081 <https://doi.org/10.5067/4DQ54OUIJ9DL>, 2021.

1082 Peng, S., Wen, D., He, N., Yu, G., Ma, A., & Wang, Q. (2016). Carbon storage in China's forest ecosystems:
 1083 estimation by different integrative methods. *Ecol. Evol.*, 6, 3129-3145

1084 Ploton, P., Mortier, F., Réjou-Méchain, M., Barbier, N., Picard, N., Rossi, V., Dormann, C., Cornu, G., Viennois,
 1085 G., Bayol, N., Lyapustin, A., Gourlet-Fleury, S., & Péliissier, R. (2020). Spatial validation reveals poor predictive
 1086 performance of large-scale ecological mapping models. *Nat. Commun.*, 11, 4540

1087 Potapov, P., Hansen, M. C., Kommareddy, I., Kommareddy, A., Turubanova, S., Pickens, A., Adusei, B., Tyukavina,
 1088 A., & Ying, Q. (2020). Landsat Analysis Ready Data for Global Land Cover and Land Cover Change Mapping.
 1089 *Remote Sens.*, 12

1090 Qi, Y., Wei, W., Chen, C., & Chen, L. (2019). Plant root-shoot biomass allocation over diverse biomes: A
 1091 global synthesis. *Glob Ecol. Conserv.*, 18, e00606, <https://doi.org/10.1016/j.gecco.2019.e00606>, 2019.

1092 Qiu, Z., Feng, Z., Song, Y., Li, M., & Zhang, P. (2020). Carbon sequestration potential of forest vegetation in China
 1093 from 2003 to 2050: Predicting forest vegetation growth based on climate and the environment. *J. Clean. Prod.*,
 1094 252, 119715

1095 Reich, P. B., Luo, Y., Bradford, J. B., Poorter, H., Perry, C. H., & Oleksyn, J. (2014). Temperature drives
 1096 global patterns in forest biomass distribution in leaves, stems, and roots. *P. Natl. Acad. Sci. USA*, 111, 13721,
 1097 <https://doi.org/10.1073/pnas.1216053111>, 2014.

1098 Roerink, G. J., Menenti, M., & Verhoef, W. (2000). Reconstructing cloudfree NDVI composites using Fourier
 1099 analysis of time series. *International Journal of Remote Sensing*, 21, 1911-1917

1100 Saatchi, S. S., Harris, N. L., Brown, S., Lefsky, M., Mitchard, E. T. A., Salas, W., Zutta, B. R., Buermann, W.,
 1101 Lewis, S. L., Hagen, S., Petrova, S., White, L., Silman, M., & Morel, A. (2011). Benchmark map of forest
 1102 carbon stocks in tropical regions across three continents. *P. Natl. Acad. Sci. USA*, 108, 9899,
 1103 <https://doi.org/10.1073/pnas.1019576108>, 2011.

1104 Santoro, M., & Cartus, O. (2019). ESA Biomass Climate Change Initiative (Biomass_cci): Global datasets of forest
 1105 above-ground biomass for the year 2017, v1. In *Centre for Environmental Data Analysis*

1106 Santoro, M., & Cartus, O. (2021). ESA Biomass Climate Change Initiative (Biomass_cci): Global datasets of forest
 1107 above-ground biomass for the years 2010, 2017 and 2018, v3. In *Centre for Environmental Data Analysis*

1108 Santoro, M., Cartus, O., Carvalhais, N., Rozendaal, D. M. A., Avitabile, V., Araza, A., de Bruin, S., Herold, M.,
 1109 Quegan, S., Rodríguez-Veiga, P., Balzter, H., Carreiras, J., Schepaschenko, D., Korets, M., Shimada, M., Itoh, T.,
 1110 Moreno Martínez, Á., Cavlovic, J., Cazzolla Gatti, R., da Conceição Bispo, P., Dewnath, N., Labrière, N., Liang,
 1111 J., Lindsell, J., Mitchard, E. T. A., Morel, A., Pacheco Pascagaza, A. M., Ryan, C. M., Slik, F., Vaglio Laurin, G.,
 1112 Verbeeck, H., Wijaya, A., & Willcock, S. (2021). The global forest above-ground biomass pool for 2010
 1113 estimated from high-resolution satellite observations. *Earth Syst. Sci. Data*, 13, 3927-3950.

带格式的: 段落间距段前: 8.15 磅, 段后: 0 磅

带格式的: 段落间距段前: 8.15 磅, 段后: 0 磅

带格式的: 段落间距段前: 8.15 磅, 段后: 0 磅

带格式的: 段落间距段前: 8.15 磅, 段后: 0 磅

1114 <https://doi.org/10.5194/essd-13-3927-2021>, 2021.

1115 Simard, M., Pinto, N., Fisher, J.B., & Baccini, A. (2011). Mapping forest canopy height globally with spaceborne
1116 lidar. *J. Geophys. Res. Biogeophys.*, 116

1117 Spawn, S. A., Sullivan, C. C., Lark, T. J., & Gibbs, H. K. (2020). Harmonized global maps of above and
1118 belowground biomass carbon density in the year 2010. *Sci. Data*, 7, 112. [https://doi.org/10.1038/s41597-020-](https://doi.org/10.1038/s41597-020-0444-4)
1119 [0444-4](https://doi.org/10.1038/s41597-020-0444-4), 2020.

1120 Stegen, J.C., Swenson, N.G., Enquist, B.J., White, E.P., Phillips, O.L., Jørgensen, P.M., Weiser, M.D., Monteagudo
1121 Mendoza, A., & Núñez Vargas, P. (2011). Variation in above-ground forest biomass across broad climatic gradients.
1122 *Global Ecol. Biogeogr.*, 20, 744-754

1123 Su, Y., Guo, Q., Xue, B., Hu, T., Alvarez, O., Tao, S., & Fang, J. (2016). Spatial distribution of forest
1124 aboveground biomass in China: Estimation through combination of spaceborne lidar, optical imagery, and forest
1125 inventory data. *Remote. Sens. Environ.*, 173, 187-199. <https://doi.org/10.1016/j.rse.2015.12.002>, 2016.

1126 Sun, X., Wang, G., Huang, M., Chang, R., & Ran, F. (2016). Forest biomass carbon stocks and variation in Tibet's
1127 carbon dense forests from 2001 to 2050. *Sci. Rep.*, 6, 34687

1128 Tang, X., Zhao, X., Bai, Y., Tang, Z., Wang, W., Zhao, Y., Wan, H., Xie, Z., Shi, X., Wu, B., Wang, G., Yan, J., Ma,
1129 K., Du, S., Li, S., Han, S., Ma, Y., Hu, H., He, N., Yang, Y., Han, W., He, H., Yu, G., Fang, J., & Zhou, G.
1130 (2018). Carbon pools in China's terrestrial ecosystems: New estimates based on an intensive field survey. *P. Natl.*
1131 *Acad. Sci. USA*, 115, 4021. <https://doi.org/10.1073/pnas.1700291115>, 2018.

1132 Thurner, M., Beer, C., Santoro, M., Carvalhais, N., Wutzler, T., Schepaschenko, D., Shvidenko, A., Kompter, E.,
1133 Ahrens, B., Levick, S.R., & Schimmlius, C. (2014). Carbon stock and density of northern boreal and temperate
1134 forests. *Global Ecol. Biogeogr.*, 23, 297-310

1135 Tong, X., Brandt, M., Yue, Y., Horion, S., Wang, K., Keersmaecker, W. D., Tian, F., Schurgers, G., Xiao, X., Luo,
1136 Y., Chen, C., Myneni, R., Shi, Z., Chen, H., and Fensholt, R.: Increased vegetation growth and carbon stock in
1137 China karst via ecological engineering. *Nat. Sustain.*, 1, 44-50. <https://doi.org/10.1038/s41893-017-0004-x>, 2018.

1138 Tong, X., Brandt, M., Yue, Y., Ciais, P., Rudbeck Jepsen, M., Penuelas, J., Wigneron, J.-P., Xiao, X., Song, X.-P.,
1139 Horion, S., Rasmussen, K., Saatchi, S., Fan, L., Wang, K., Zhang, B., Chen, Z., Wang, Y., Li, X., & Fensholt,
1140 R. (2020). Forest management in southern China generates short term extensive carbon sequestration. *Nat.*
1141 *Commun.*, 11, 129. <https://doi.org/10.1038/s41467-019-13798-8>, 2020.

1142 Tong, X., Brandt, M., Yue, Y., Horion, S., Wang, K., Keersmaecker, W.D., Tian, F., Schurgers, G., Xiao, X., Luo,
1143 Y., Chen, C., Myneni, R., Shi, Z., Chen, H., & Fensholt, R. (2018). Increased vegetation growth and carbon stock
1144 in China karst via ecological engineering. *Nat. Sustain.*, 1, 44-50

1145 Verger, A., Baret, F., & Weiss, M. (2014). Near-Real-Time Vegetation Monitoring at Global Scale. *IEEE Journal*
1146 *of Selected Topics in Applied Earth Observations and Remote Sensing*, 7, 3473-3481

1147 Wang, J., Feng, L., Palmer, P. I., Liu, Y., Fang, S., Bösch, H., O'Dell, C. W., Tang, X., Yang, D., Liu, L., & Xia,
1148 C. (2020). Large Chinese land carbon sink estimated from atmospheric carbon dioxide data. *Nature*, 586, 720-
1149 723. <https://doi.org/10.1038/s41586-020-2849-9>, 2020.

带格式的: 段落间距段前: 8.15 磅, 段后: 0 磅

带格式的: 段落间距段前: 8.15 磅, 段后: 0 磅

带格式的: 段落间距段前: 8.15 磅, 段后: 0 磅

带格式的: 段落间距段前: 8.15 磅, 段后: 0 磅

带格式的: 段落间距段前: 8.15 磅, 段后: 0 磅

1150 Wang, L., Li, L., Chen, X., Tian, X., Wang, X., & Luo, G. (2014). Biomass Allocation Patterns across China's
1151 Terrestrial Biomes. *PLoS One*, 9, e93566. <https://doi.org/10.1371/journal.pone.0093566>, 2014.

1152 Wigneron, J.-P., Li, X., Wang, M., Fan, L., Frappart, F., Fan, L., Al-Yaari, A., De Lannoy, G., Liu, X., Ciais, P., Sun,
1153 R., Liu, Y., Li, X., Liu, X., Moisy, C., and Wigneron, J.-P.: An alternative AMSR2 vegetation optical depth for
1154 monitoring vegetation at large scales. *Remote Sens. Environ.*, 263, 112556.
1155 <https://doi.org/10.1016/j.rse.2021.112556>, 2021a.

1156 Wang, M., Le-Masson, E., & Wigneron, J.-P., Sun, R., Fan, L., Frappart, F., Tao, S., Chai, L., Li, X., Liu, X., Ma,
1157 H., Moisy, C. (2021). SMOS-IC data, and Ciais, P.: A consistent record of vegetation optical depth retrieved from
1158 the AMSR-E and AMSR2 X-band observations. *Int. J. Appl. Earth Obs.*, 105, 102609.
1159 <https://doi.org/10.1016/j.jag.2021.102609>, 2021b.

1160 Wigneron, J.-P., Chanzy, A., Calvet, J.-C., and Bruguier, N.: A simple algorithm to retrieve soil moisture and L
1161 VOD: Historical development, applications and perspectives. *vegetation biomass using passive microwave*
1162 *measurements over crop fields*, *Remote Sens. Environ.*, 254, 112238. *Sens. Environ.*, 51, 331-341,
1163 [https://doi.org/10.1016/0034-4257\(94\)00081-W](https://doi.org/10.1016/0034-4257(94)00081-W), 1995.

1164 Xu, B., Guo, Z., Piao, S., & Fang, J. (2010). Biomass carbon stocks in China's forests between 2000 and 2050: A
1165 prediction based on forest biomass age relationships. *Science China Life Sciences*, 53, 776-783

1166 Wu, X., Wang, S., Fu, B., Feng, X., and Chen, Y.: Socio-ecological changes on the Loess Plateau of China after
1167 Grain to Green Program. *Sci. Total Environ.*, 678, 565-573. <https://doi.org/10.1016/j.scitotenv.2019.05.022>, 2019.

1168 Xu, L., Saatchi, S. S., Yang, Y., Yu, Y., Pongratz, J., Bloom, A. A., Bowman, K., Worden, J., Liu, J., Yin, Y., Domke,
1169 G., McRoberts, R. E., Woodall, C., Nabuurs, G.-J., de-Miguel, S., Keller, M., Harris, N., Maxwell, S., &
1170 Schimel, D. (2021). Changes in global terrestrial live biomass over the 21st century. *Sci. Adv.*, 7, eabe9829,
1171 <https://doi.org/10.1126/sciadv.abe9829>, 2021.

1172 Xu, L., Yu, G., He, N., Wang, Q., Gao, Y., Wen, D., Li, S., Niu, S., & Ge, J. (2018). Carbon storage in China's
1173 terrestrial ecosystems: A synthesis. *Sci. Rep.*, 8, 2806

1174 Yang, D., Liu, Y., Feng, L., Wang, J., Yao, L., Cai, Z., Zhu, S., Lu, N., & Lyu, D. (2021). The First Global
1175 Carbon Dioxide Flux Map Derived from TanSat Measurements. *Ad. Atmos. Sci.*, 38, 1433-1443,
1176 <https://doi.org/10.1007/s00376-021-1179-7>, 2021.

1177 Yang, X., Guo, Y., Mohhamot, A., Liu, H., Ma, W., Yu, S., & Tang, Z. (2017). Distribution of biomass in relation
1178 to environments in shrublands of temperate China. *Chinese Journal of Plant Ecology*, 41, 22-30

1179 Yao, Y., Piao, S., & Wang, T. (2018). Future biomass carbon sequestration capacity of Chinese forests. *Sci. Bull.*,
1180 63, 1108-1117

1181 Yin, G., Zhang, Y., Sun, Y., Wang, T., Zeng, Z., & Piao, S. (2015). MODIS Based Estimation of Forest
1182 Aboveground Biomass in China. *PLoS One*, 10, e0130143

1183 Yang, J. and Huang, X.: The 30 m annual land cover dataset and its dynamics in China from 1990 to 2019, *Earth*
1184 *Syst. Sci. Data*, 13, 3907-3925. <https://doi.org/10.5194/essd-13-3907-2021>, 2021.

带格式的: 段落间距段前: 8.15 磅, 段后: 0 磅

带格式的: 段落间距段前: 8.15 磅, 段后: 0 磅

带格式的: 段落间距段前: 8.15 磅, 段后: 0 磅

1185 [Yu, Z., Zhao, H., Liu, S., Zhou, G., Fang, J., Yu, G., Tang, X., Wang, W., Yan, J., Wang, G., Ma, K., Li, S., Du, S.,](#)
1186 [Han, S., Ma, Y., Zhang, D., Liu, J., Liu, S., Chu, G., Zhang, Q., and Li, Y.:](#) Mapping forest type and age in China's
1187 [plantations. Sci. Total Environ., 744, 140790, <https://doi.org/10.1016/j.scitotenv.2020.140790>, 2020.](#)

1188 Zhang, R., Zhou, X., Ouyang, Z., Avitabile, V., Qi, J., Chen, J., [&and](#) [Giannico, V.](#) ~~(2019).~~ Estimating
1189 aboveground biomass in subtropical forests of China by integrating multisource remote sensing and ground data,
1190 Remote. Sens. Environ., 232, 111341, <https://doi.org/10.1016/j.rse.2019.111341>, 2019.

1191 ~~Zhang, Y., & Liang, S. (2020). Fusion of Multiple Gridded Biomass Datasets for Generating a Global Forest~~
1192 ~~Aboveground Biomass Map. Remote Sens., 12~~

1193 Zhang, Y., Yao, Y., Wang, X., Liu, Y., [&and](#) [Piao, S.](#) ~~(2017).~~ Mapping spatial distribution of forest age in China,
1194 Earth Space Sci., 4, 108-116, <https://doi.org/10.1002/2016EA000177>, 2017.

1195

带格式的: 段落间距段前: 8.15 磅, 段后: 0 磅

带格式的: 段落间距段前: 8.15 磅, 段后: 0 磅